JGR Space Physics

RESEARCH ARTICLE
10.1029/2024JA033253

Reliability of Matching AMPERE Field-Aligned Current Boundaries With SuperDARN Lower Latitude Ionospheric Convection Boundaries During Geomagnetic Storms

M.-T. Walach[1], A. R. Fogg[2], J. C. Coxon[3], A. Grocott[1], S. E. Milan[4], H. K. Sangha[5], K. A. McWilliams[6], S. K. Vines[7], M. Lester[4], and B. J. Anderson[8]

[1]Lancaster University, Physics Department, Lancaster, UK, [2]School of Cosmic Physics, DIAS Dunsink Observatory, Dublin Institute for Advanced Studies, Dublin 15, Ireland, [3]Department of Mathematics, Physics and Electrical Engineering, Northumbria University, Newcastle Upon Tyne, UK, [4]University of Leicester, Department of Physics and Astronomy, Leicester, UK, [5]UK Space Agency, Harwell, UK, [6]University of Saskatoon, Saskatoon, SK, Canada, [7]Southwest Research Institute, San Antonio, TX, USA, [8]Johns Hopkins University Applied Physics Laboratory, Laurel, MD, USA

Abstract High-latitude ionospheric convection is a useful diagnostic of solar wind-magnetosphere interactions and nightside activity in the magnetotail. For decades, the high-latitude convection pattern has been mapped using the Super Dual Auroral Radar Network (SuperDARN), a distribution of ground-based radars which are capable of measuring line-of-sight (l-o-s) ionospheric flows. From the l-o-s measurements an estimate of the global convection can be obtained. As the SuperDARN coverage is not truly global, it is necessary to constrain the maps when the map fitting is performed. The lower latitude boundary of the convection, known as the Heppner-Maynard boundary (HMB), provides one such constraint. In the standard SuperDARN fitting, the HMB location is determined directly from the data, but data gaps can make this challenging. In this study we evaluate if the HMB placement can be improved using data from the Active Magnetosphere and Planetary Electrodynamics Response Experiment (AMPERE), in particular for active time periods when the HMB moves to latitudes below 55°. We find that the boundary as defined by SuperDARN and AMPERE are not always co-located. SuperDARN performs better when the AMPERE currents are very weak (e.g., during non-active times) and AMPERE can provide a boundary when there is no SuperDARN scatter. Using three geomagnetic storm events, we show that there is agreement between the SuperDARN and AMPERE boundaries but the SuperDARN-derived convection boundary mostly lies ∼3° equatorward of the AMPERE-derived boundary. We find that disagreements primarily arise due to geometrical factors and a time lag in expansions and contractions of the patterns.

Plain Language Summary The high-latitude ionosphere, a part of Earth's upper atmosphere filled with ions and electrons, moves in response to solar wind and other space weather activities. This movement, known as ionospheric convection, is key to understanding how magnetic fields and plasma interact in space. To study this, scientists use the Super Dual Auroral Radar Network (SuperDARN), a ground-based system designed to measure these ionospheric movements. For years, researchers have questioned whether the methods used to combine SuperDARN data into convection maps are the best they can be. A crucial part of this process is determining the point at lower latitudes, where convection slows down. This can be done using SuperDARN data or data from spacecraft. For example, data from the Active Magnetosphere and Planetary Electrodynamics Response Experiment (AMPERE) from the Iridium satellites can be used for this. AMPERE provides a measure of the electric currents that are associated with the convection. We compare two methods with ground-based radars and spacecraft, to see if the boundaries match. The main finding is that they often do not, with the spacecraft and radar data showing different convection boundaries. This disagreement challenges our understanding of plasma physics, as both methods should ideally show similar results.

Key Points:

- When SuperDARN data coverage is good, agreement can be found between the Heppner-Maynard boundary and the field-aligned current boundary
- The Heppner-Maynard boundary often lies 3° equatorward of the field-aligned current boundary
- Poor agreement tends to stem from poor data coverage or asymmetries in the field-aligned currents

Supporting Information:

Supporting Information may be found in the online version of this article.

Correspondence to:

M.-T. Walach,
m.walach@lancaster.ac.uk

Citation:

Walach, M.-T., Fogg, A. R., Coxon, J. C., Grocott, A., Milan, S. E., Sangha, H. K., et al. (2025). Reliability of matching AMPERE field-aligned current boundaries with SuperDARN lower latitude ionospheric convection boundaries during geomagnetic storms. *Journal of Geophysical Research: Space Physics*, *130*, e2024JA033253. https://doi.org/10.1029/2024JA033253

Received 30 AUG 2024
Accepted 14 JAN 2025

Author Contributions:

Conceptualization: M.-T. Walach, A. R. Fogg, M. Lester
Data curation: M.-T. Walach, A. R. Fogg, S. E. Milan, K. A. McWilliams, S. K. Vines, B. J. Anderson
Formal analysis: M.-T. Walach, A. R. Fogg, J. C. Coxon
Funding acquisition: M.-T. Walach, A. Grocott
Investigation: M.-T. Walach, A. R. Fogg, J. C. Coxon, S. E. Milan, S. K. Vines, B. J. Anderson
Methodology: M.-T. Walach, A. R. Fogg, J. C. Coxon, S. E. Milan, M. Lester
Project administration: M.-T. Walach, A. R. Fogg

1. Introduction

Plasma circulates in the terrestrial magnetosphere due to the Dungey cycle, whereby reconnection on the dayside of the magnetosphere opens magnetic flux and nightside reconnection in the magnetotail closes magnetic flux (Dungey, 1961, 1963). Since ionospheric plasma can be largely said to be frozen-in (i.e., it circulates with the magnetic flux), the ionosphere also follows this circulation pattern. This is known as

Resources: M.-T. Walach, A. Grocott, K. A. McWilliams, S. K. Vines, B. J. Anderson
Software: M.-T. Walach, A. R. Fogg, S. E. Milan, H. K. Sangha
Validation: M.-T. Walach, A. R. Fogg, J. C. Coxon, S. K. Vines
Visualization: M.-T. Walach, A. R. Fogg, J. C. Coxon, S. E. Milan, H. K. Sangha
Writing – original draft: M.-T. Walach, A. R. Fogg
Writing – review & editing: M.-T. Walach, A. R. Fogg, J. C. Coxon, A. Grocott, S. E. Milan, H. K. Sangha, K. A. McWilliams, S. K. Vines, M. Lester

'convection'. On average, the reconnection-driven plasma flows generate a dual-cell convection pattern in the ionosphere (e.g., Obayashi & Nishida, 1968; Heppner, 1972; Stern, 1977; Heppner & Maynard, 1987, and references within). Plasma flows from the dayside to the nightside across the pole and returns via the dusk and dawn sides at lower latitudes. Ionospheric convection is a key indicator of the state of the magnetosphere. Due to the solar wind-magnetosphere-ionosphere coupling, the plasma convection in the ionosphere changes in response to changes in the solar wind driving and magnetospheric response (as explicitly shown by Walach et al., 2017). The ionosphere also responds to changes in the magnetosphere, which may not be in direct response to solar wind drivers. Substorms, which result from reconnection in the magnetotail, are at times an example of this. Substorms can accelerate plasma flows in the ionosphere and change the geometry of convection (Bristow & Jensen, 2007; Heppner, 1972; Provan et al., 2004).

Electric currents flow due to deformations in the Earth's magnetic fields, which make it non-dipolar (Milan et al., 2017; Parker, 1996, 1997; Vasyliunas, 2001, 2005). Within the magnetosphere, currents are thought to connect the ionosphere to the magnetopause and the ring current (Iijima & Potemra, 1978). These are known as Birkeland currents (Birkeland, 1908, 1913) or field-aligned currents (FACs). In the ionosphere, they can be split into two interlaced systems: the region 1 (R1) and region 2 (R2) currents, which are connected through the conducting ionosphere. The R1 currents form a rough oval around the magnetic pole with current flowing away from the ionosphere on the dusk side and current flowing into the ionosphere on the dawn side. The R2 currents flow at a lower latitude than the R1 currents and also form a roughly concentric ring. The R2 currents flow in opposite directions up and down the field lines to their neighboring R1 currents and form a pair of semi-circles (e.g., Coxon et al., 2014; Coxon et al., 2018). The locations where the FACs flow into and out of the ionosphere can be described in terms of convection vorticity and hence, when we assume a uniform conductivity, they must match where the plasma flows change direction theoretically (Sofko et al., 1995). The R1 currents are also co-located with the boundary between the open and closed field lines (Clausen et al., 2013; Cowley & Lockwood, 1992; Lockwood, 1991; Milan et al., 2017), but whilst the R1 currents provide a fuzzy boundary, the boundary between open and closed field lines is discrete.

FACs can also be present in the magnetosphere due to field line resonances, and these can generate auroras (e.g., Milan et al., 2001; Rankin et al., 2005). Using magnetohydrodynamic (MHD) wave coupling and phase mixing in a model of the magnetosphere, FACs currents which resemble the R1 and R2 systems can be modeled (e.g., Elsden et al., 2022; Wright & Elsden, 2020). This MHD modeling shows that during geomagnetic storms, the FACs and field line resonances which are located outside the plasmasphere, move closer to the Earth (Elsden et al., 2022).

Furthermore, the aurora is expected to be colocated with the FACs (Carter et al., 2016). For example, McWilliams et al. (2001) used Super Dual Auroral Radar Network (SuperDARN) measurements of ionospheric plasma vorticity to estimate the FAC per unit Pedersen conductance and found that the upward FACs were colocated with auroral emission from the Polar Visible Imaging System (VIS) in the post-noon sector.

Theoretically, the equatorward edge of the locations where R2 currents flow should match with the equatorial convection boundary (e.g., Milan et al., 2017, and references therein). Using FACs inferred from ground magnetometers, Weygand et al. (2023) correlated the magnetic latitudes of these equatorward boundaries with a variety of parameters and showed that the highest correlation is found with IMF B_Z. Further, Weygand et al. (2023) showed that the next most important correlations of the equatorward boundary latitude are found to be with the SYM-H index and the mean solar wind electric field with respect to the reference frame of earth (VB_Z). Their study also showed that during storms, the equatorward boundary extends to 45° magnetic latitude.

Data from SuperDARN coherent ionospheric scatter radars can be used to build large-scale maps of ionospheric convection and they provide a rich data set, having been running since the 1990s (Chisham et al., 2007; Greenwald et al., 1995; Lester, 2008; Nishitani et al., 2019). The radars are able to measure line-of-sight ionospheric velocities and we combine the data to make convection maps following the procedure initially outlined by Ruohoniemi and Baker (1998), and often termed the "map potential technique". One step in this process, discussed in detail by Shepherd and Ruohoniemi (2000), is to fit a lower-latitude boundary to the convection, which is known as the Heppner-Maynard Boundary (HMB). In the SuperDARN fitting process, the HMB has a form which is circular on the nightside and tapers off to higher latitudes on the dayside. Shepherd and Ruohoniemi (2000) chose this form after a statistical study by Heppner and Maynard (1987) who found that the ovoid shape on the dayside together with the circular shape on the nightside is a better fit for the HMB than a simple

circle. In the standard SuperDARN fitting technique, the HMB is chosen at 1° below the lowest latitude where at least three SuperDARN flow vectors reach above 100 m/s (SuperDARN Data Analysis Working Group, Thomas, Ponomarenko, Bland, et al., 2018). However, this can lead to inconsistencies, since SuperDARN backscatter is not always present everywhere due technical, as well as, geophysical reasons. This technique is conventionally used when making convection maps and is what we use in this study. See Section 2 for further details of the SuperDARN fitting algorithm.

The HMB sits at the lower latitude of the convection cells, where the electric field theoretically goes to zero. Imber et al. (2013a) studied the HMB measured by SuperDARN and found that, on average, it lies just a few degrees equatorward of the latitude where the auroral oval is brightest. In their study, Imber et al. (2013a) considered data from 2000 to 2002 where SuperDARN data was available at the same time as auroral data as from the Imager for Magnetopause-to-Aurora Global Exploration (IMAGE) satellite, which allowed for a systematic study of the two boundaries. The results showed that the two are often systematically offset. The average measured offset was 2.2°, with the auroral latitude lying 0–3° poleward of the HMB during ∼55% of the 2 min intervals. Imber et al. (2013a) also noted that larger offsets often correspond to substorm or geomagnetic storm times. It is worth noting that for the time period of data analyzed by Imber et al. (2013a), no mid-latitude data was available. As was shown by Walach et al. (2021) mid-latitude radar data are important when choosing the HMB.

Fogg et al. (2020) used FAC data from the Active Magnetosphere and Planetary Electrodynamics Response Experiment (AMPERE, Anderson et al., 2000; Anderson et al., 2014; Waters et al., 2001; Coxon et al., 2018) to show that there is a statistical relationship between the boundary between R1 and R2 and the HMB. The relationship from Fogg et al. (2020) was developed as an alternative for the HMB used for the SuperDARN fitting algorithm. Fogg et al. (2020) used data from the solar minimum and maximum (2011 and 2015, respectively) to match the R1/R2 FAC location to the SuperDARN HMB. This yielded a linear relationship, which can be used as an input into the SuperDARN fitting, when AMPERE R1/R2 boundaries are available. Walach and Grocott (2019) and Walach et al. (2021) found however that during geomagnetic storms, the HMB moves to lower latitudes than previously thought. Similarly, Coxon et al. (2017) showed that the R2 current intensifies during substorms, which implies that the HMB is also lowered during substorms as was indeed shown by Bristow and Jensen (2007) using SuperDARN data. Whilst Coxon et al. (2023) showed that the most intense currents measured by AMPERE were found on the dayside, the currents shown in their study also expanded to lower latitudes during geomagnetic storms. Walach and Grocott (2019) found that the convection can expand to as low as 40° magnetic latitude during geomagnetic storms as measured by SuperDARN, which is the current observational SuperDARN limit. Conversely to the 45° limit found by Weygand et al. (2023), the saturation of data points at the observational limit found by Walach and Grocott (2019) suggests that the equatorward boundary of the convection is likely to reach even lower than 40° magnetic latitude. Similar to Weygand et al. (2023), Walach, Grocott, Staples, and Thomas (2022) also showed that the HMB moves to lower latitudes with increased SYM-H. However, the relationship breaks down for extremely negative values of SYM-H, which is likely due to the observational limit of the mid-latitude radars constraining the HMB. Prior to mid-latitude SuperDARN data being available (e.g., data analyzed by Imber et al., 2013b; Imber et al., 2013a), the HMB limit was located at 50° latitude, which would have misplaced ∼19% of the HMBs during geomagnetic storms (Walach & Grocott, 2019).

Since the data from Fogg et al. (2020) did not explicitly include any geomagnetic storms, the question remains: Is the field aligned current-derived boundary location a good proxy for the SuperDARN ionospheric convection boundary during storms? If the data from Fogg et al. (2020) can be extrapolated linearly, we may expect the answer to be a simple 'yes', but Walach, Grocott, Staples, and Thomas (2022) showed that the HMB behaves non-linearly with increasing geomagnetic activity. If field-aligned current is not always a good proxy, what controls this? We expect the magnetosphere to behave differently during geomagnetic storms. The ring current, for example, is enhanced and the inner magnetosphere changes, which affects the boundary between the convecting and non-convecting plasma (i.e., the plasmapause) (Elsden et al., 2022; Gonzalez et al., 1994; Pierrard et al., 2021; Sandhu, Rae, Staples, et al., 2021; Sandhu, Rae, & Walach, 2021; Sandhu, Rae, Wygant, et al., 2021; Wharton et al., 2020).

Where the HMB or convection boundary is truly located and how this relates to the R1 and R2 currents is further complicated by time-varying phenomena. For example, Sangha et al. (2020) showed that the R2 FACs can bifurcate into two channels and the lower latitude branch can split off. Sangha et al. (2020) relates the later stages of bifurcations with evidence for Subauroral polarization streams (SAPS). SAPS create large plasma flows and

electric fields in the sub-auroral ionosphere and are thus of interest to Space Weather. Sangha et al. (2020) showed that bifurcations commonly lead to SAPS and are more likely to occur during substorms. The bifurcations originate in the R2 FACs, and hence these bifurcations are tied to the convection pattern at some point prior to connecting to a SAPS. Understanding when they separate from the R2 region and at what point they become an ionospheric plasma flow phenomenon which is latitudinally separate from the dual-cell convection is important to understanding the relationship between the HMB and the FAC systems,and thus the coupled magnetosphere and ionosphere.

In this study, we compare the FAC location to the SuperDARN convection maps during some case studies to determine if the linear relationship found by Fogg et al. (2020) can be extrapolated to include more active times, such as geomagnetic storms. We have identified three events in which the HMB moves to low latitudes (∼40°). As such, the Fogg et al. (2020) algorithm was not trained on this data and we can see how it performs against the SuperDARN maps. The solar wind driving and resulting geomagnetic conditions are shown in Figures S1–S3 in Supporting Information S1. These show that we study a variety of conditions leading to geomagnetic storms of varying strength with the first one being the weakest storm and the last one being the strongest. In Section 2 we describe the data used in this study, in Section 3 we present data in the format of three case studies and in Section 4 we discuss these results.

2. Data

2.1. SuperDARN

SuperDARN is a network of coherent radars which were built to remotely sense convection in the ionosphere. Their line of sight convection measurements can be combined to make convection maps. These SuperDARN convection maps provide a quantitative representation of the convection field in the high-latitude ionosphere. This is achieved by fitting spherical harmonic functions to line-of-sight velocities collected by the radars (e.g., Chisham et al., 2007; Nishitani et al., 2019). Different methods for fitting the convection maps exist and in this study we use a standard method introduced and benchmarked against other techniques by Walach, Grocott, Staples, and Thomas (2022). In Walach, Grocott, Staples, and Thomas (2022) five data sets were studied (D0-D4) and we use the final data set D4 in this study. The D4 data set includes all radars in the Northern Hemisphere and was processed using the Radar Software Toolkit v4.2 (SuperDARN Data Analysis Working Group, Thomas, Ponomarenko, Billett, et al., 2018) with the Thomas and Shepherd (2018) background model. For more information on how this data set was processed and compares to older convection maps, measured parameters and dusk-dawn asymmetries, we refer the reader to Walach, Grocott, Staples, and Thomas (2022); Walach, Grocott, Thomas, and Staples (2022). This convection map data set is simply referred to as the SuperDARN data in what follows and all vectors shown are the velocities from the spherical harmonic fitting procedure (Ruohoniemi & Baker, 1998).

The most important processing step for this study is how we choose the HMB. We will refer to the SuperDARN HMB as Λ_{Walach} throughout this study. This was fitted using the SuperDARN processing technique whereby the algorithm uses the data to find the HMB. The algorithm places the HMB at 1° below the lowest latitude where a minimum number of backscatter echoes are above a certain velocity threshold. In the SuperDARN processing, these values can be adjusted. We use a threshold of 100 m/s and the minimum number of vectors which has to be above this minimum magnitude is three, a commonly used combination (e.g., Walach, Grocott, Staples, & Thomas, 2022), and the same criterion as originally defined by Shepherd and Ruohoniemi (2000).

2.2. AMPERE

AMPERE is a data set which captures FACs in both the northern and southern hemispheres (Anderson et al., 2000, 2014, 2021; Waters et al., 2001, 2020). AMPERE current densities are determined from engineering magnetometers on 66 Iridium telecommunications satellites. The AMPERE data set is continuous, and provides a map of radial current density in a 1 hr MLT by 1° latitude grid for both hemispheres. Because the Iridium satellites are at 780 km altitude, the full AMPERE grid is resampled every 10 min. Spherical harmonic fitting is performed at every 2-min over a sliding 10-min accumulation window (see Waters et al. (2020) for more details), so the data can be provided at 2 min resolution to aid comparison with SuperDARN data. A review of AMPERE research is available at Coxon et al. (2018). Both the AMPERE data set and the Spherical Elementary Current System method

employed for example, by Weygand et al. (2023) calculate vertical current density, and using this as a measure of field-aligned current assumes that the field lines are vertical.

The boundary between the R1 and R2 currents (from here on "R1/R2 boundary") was determined from AMPERE data using the method described by Milan et al. (2015), which will be summarized here. The FAC strength is integrated over circles of different radii and with different circle center locations, and due to the R1/R2 pattern (upward then downward current or vice versa, depending on MLT) a bipolar signature is observed over increasing radius. The circle radius and center location with the largest peak-to-peak bipolar signature is chosen as the circle intersecting the R1 and R2 currents. The latitude at which this boundary intersects the midnight meridian should be equivalent to the boundary where the flows reverse. We have therefore named this the return flow boundary, or in short: R_F.

Using values of R_F provided by Milan (2019), Fogg et al. (2020) determined a linear relationship between R_F and the midnight meridian latitude of the SuperDARN Heppner-Maynard Boundary (HMB). They provide equations to calculate corrected values of the HMB midnight meridian latitude (hereafter referred to as Λ_{Fogg}) based on this linear relationship, which are used to calculate the set of Λ_{Fogg} values (Fogg, 2020) used in this paper. The boundary from Fogg et al. (2020) uses the same standard SuperDARN HMB shape SuperDARN (Shepherd & Ruohoniemi, 2000), because the Fogg method was developed as an alternative to the SuperDARN HMB fitting. The Fogg et al. (2020) fitting excluded very active periods, so in this paper we purposefully compare geomagnetic storms to see if their result can be extrapolated to active periods.

3. Results

In this section we present data from the three individual event case studies and compare the locations of the SuperDARN-derived HMB (Λ_{Walach}) with the locations of the R_F boundary and the linear fit for the R_F-derived corrected HMB midnight meridian latitude (Λ_{Fogg}). These cases are representative of geomagnetic storm times when Λ_{Walach} goes to lower latitudes than is typical (40–50°) and the number of gridded from SuperDARN ≥250 (Walach, Grocott, Staples, & Thomas, 2022). These three events are fairly representative of features we see during highly driven times when Λ_{Walach} moves to lower latitudes and are good examples at highlighting some of the general issues we face when comparing these two data sets, which we will discuss in more detail in the following sections.

For each event, we show a 48 hr time series. We show four keograms for the AMPERE data: with a midnight-noon and a dawn-dusk slice for each hemisphere. This allows us to see rough asymmetries and how the FACs change over time. Λ_{Walach} is overlaid on top of the AMPERE data alongside Λ_{Fogg} from Fogg (2020) and the R_F boundary (Milan, 2019). Below the keograms we show the difference between Λ_{Fogg} and Λ_{Walach} and in the last panel we show the geomagnetic conditions: the Sym-H index (Iyemori, 1990), which is an indicator of ring current strength, and the AL and AU indices which show geomagnetic activity at higher latitudes (Davis & Sugiura, 1966). For each event we also show a number of polar snapshots. These show the SuperDARN convection maps and AMPERE data together and they are selected for each event to illustrate specific points. The SuperDARN convection maps show the electrostatic potentials, Λ_{Walach}, and the line-of-sight convection vectors. Overlaid on these polar snapshots is also Λ_{Fogg}. The full selection of polar plots for all three events are provided in the accompanying data archive Walach and Fogg (2024a) and the boundaries are available in the supplementary files by Walach and Fogg (2024b). Anderson et al. (2014) showed that the AMPERE data has a three-sigma level of 0.16 μA m^{-2}, so all AMPERE data below a threshold of ±0.2 μA m^{-2} have been plotted in white, and we saturate plots at ±1 μA m^{-2} to help bring out reliable features in the data.

3.1. Event 1: 20 January 2016

Figure 1 shows the four AMPERE keograms for the first case study. Figure 1a shows the northern hemisphere midnight-noon slice, Figure 1b shows the northern hemisphere dawn-dusk slice and Figures 1c and 1d show the equivalent slices for the southern hemisphere, respectively. Blue shows downward directed currents whereas red shows upward directed currents. The green line shows Λ_{Walach}, the black line shows Λ_{Fogg} and the gray line shows R_F. Figure 1e shows the difference between Λ_{Fogg} and Λ_{Walach} at midnight in the northern hemisphere. Figure 1f shows the geomagnetic conditions for this event: Sym-H indicates that a small geomagnetic storm occurs, starting

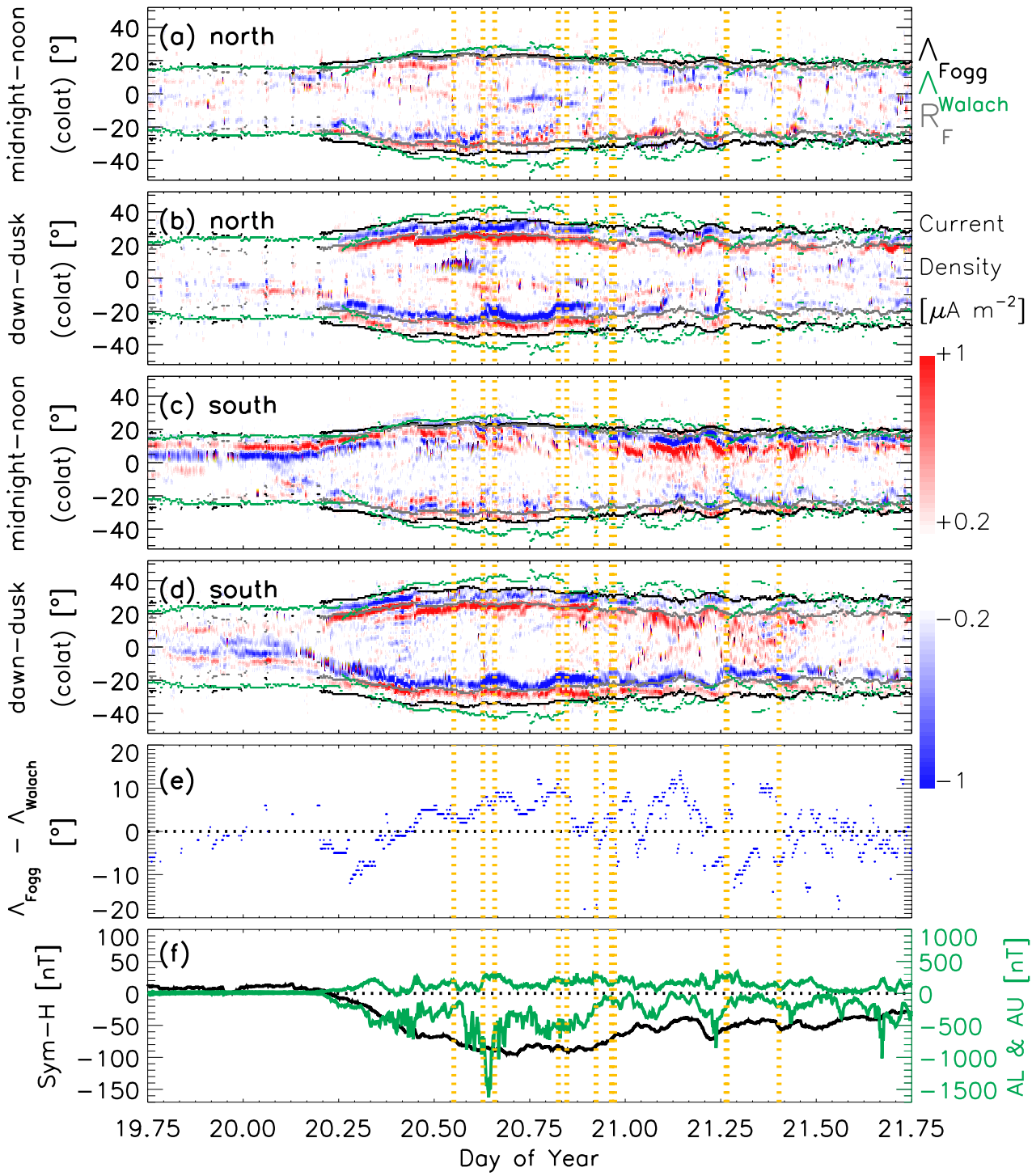

Figure 1. Six paneled plot showing keograms of the FACs and flow boundaries for 18:00 UT on 19 January 2016 to 18:00 UT on 21 January 2016: Λ_{Walach} (green), Λ_{Fogg} (black) and R_F (gray). The vertical dashed orange lines indicate the timings for the panels in Figure 2. (a) and (c) show the midnight-noon keograms for the northern and southern hemisphere, respectively. (b) and (d) show the dawn-dusk keograms for the northern and southern hemispheres, respectively. (e) shows the difference at midnight between Λ_{Fogg} and Λ_{Walach} in the northern hemisphere and panel (f) shows the geomagnetic conditions: Sym-H (black), and AL and AU (green). Each minor tick on the horizontal axis is equivalent to 1 hour and the major ticks are separated by 6 hours each.

on the 20th January and AL and AU also show a long period of geomagnetic activity, with a series of activations occurring at the same time as the Sym-H decrease. Each boundary (Λ_{Fogg} and Λ_{Walach}) will not appear at the same position on each keogram because we took the midnight meridian value, and traced it around the non-circular

boundary shape to dawn, dusk, and noon using the standard SuperDARN formulation (Shepherd & Ruohoniemi, 2000). The dashed vertical orange lines show the intervals chosen for the polar plots in Figure 2. Prior to DOY 20.25 (20 January 2016, 06:00 UT) the FACs are, at times, too weak to fit R_F and so Λ_{Fogg} is also missing at those times in Figure 1. During this time, Λ_{Walach} fits the latitudinal extent of the existing currents at noon MLT in the southern hemisphere fairly well. Around DOY 20.25, we see a strengthening of the FACs, as well as an expansion of the FACs and all boundaries to lower latitudes. After DOY 20.5 (12:00 UT on 20 January 2016) onwards Λ_{Walach} lies at around 5 to 10° lower than Λ_{Fogg} at dawn and dusk (Figures 1b and 1d) and midnight (Figures 1a and 1c).

As a general trend for this event, in Figure 1b, we see Λ_{Fogg} wraps quite tightly around the FACs at dusk and R_F is sometimes just inside the outer edge of the R1 FAC (i.e., more poleward than where it should be). Figure 1e shows that, generally for event 1, the convective flows are continuing ∼7° outside Λ_{Fogg}, with the few exceptions which we discussed, when the currents and convection are weak.

Figure 2 shows example snapshots for specifically selected times of interest. These were selected to show a variety of features, and examples where Λ_{Walach} and Λ_{Fogg} fit well or poorly. Figure 2 shows the SuperDARN and AMPERE data plotted in AACGM coordinates (Shepherd, 2014). The time indicates the start of the SuperDARN maps. The blue and red show the AMPERE current density according to the colourbar in the top right, and the black lines show equipotentials from the SuperDARN maps. The line-of-sight SuperDARN flow vectors are shown in green, where lighter vectors show lower magnitudes and darker vectors show larger magnitudes. The black dotted boundary shows Λ_{Fogg}. The thick green line shows Λ_{Walach}, with its midnight meridian latitude recorded on the bottom left of each panel. SuperDARN vectors below Λ_{Walach} are shown in black. Each panel is centered on the northern magnetic pole with noon MLT pointing toward the top of the page, dusk toward the left, midnight toward the bottom and dawn toward the right. Each hour in MLT is indicated by the dashed gray radial lines. The SuperDARN transpolar voltage or cross polar cap potential is shown on the bottom right of each panel. The number underneath (n) indicates the number of backscatter echoes. The cross and red arrow on the top right of each plot shows the projection of the IMF vector on the GSM $Y - Z$ plane. The latitude circles are separated by 10° as indicated by the colatitudes in the top right corner of each panel.

In Figure 1 we saw Λ_{Walach} lie ∼10° lower at dawn, dusk and midnight than Λ_{Fogg} and the R2 FACs. In Figure 2a, at 13:14 UT on 20 January 2016, we examine this in more detail: Overall, despite the mismatch of Λ_{Walach} lying at lower latitudes than Λ_{Fogg}, the return flow proportion of the convection pattern sits well on R2 FACs. At 15:04 UT (Figure 2b) we may be seeing something similar to a SAPS signatures included in the convection pattern: We see a current bifurcation of the R2 system at between 3 and 7 MLT with an eastward directed flow (and a weaker one between 17 and 20 MLT). Flows continue into the gap between the main R2 and the bifurcation, at ∼30° colatitude between 6-8 MLT and 2–4 MLT so this could be the start of something similar SAPS event, though we note that SAPS are usually accompanied by westward flows. After this we see repeated bifurcations throughout the interval. As already mentioned during this interval, Λ_{Walach} is around 10° outside the R2 currents. This mismatch happens because the boundary shape does not match the shape of the R2 currents. Later, at around 15:48 UT (Figure 2c), the convection continues to lie equatorward of the R2 FACs. This expansion is due to an extension of the convective dusk cell across midnight, shifting of the Harang discontinuity toward dawn similar to what was observed during substorms by Bristow et al. (2001); Bristow et al. (2003); Bristow and Jensen (2007).

Later, at 19:48 UT (Figure 2d) we see persistent, but slow moving flows in the morning sector (∼4–5 MLT). From Figure 1, we see that the R_F boundary is clearly defined, but we see from Figure 2d that the flows which have defined Λ_{Walach} are sitting far outside R2 (near 6 MLT). Figure 2e, at 20:20 UT, shows an example of very good agreement: Now, the same vectors which previously defined Λ_{Walach} (between 4 and 6 MLT) are below 100 m/s and therefore fall below Λ_{Walach}, which is now defined by vectors near 7, 11, and 12 MLT. As a result, Λ_{Walach} has moved poleward, wrapping around the FACs nicely, and the two boundaries match perfectly, despite n being lower than for panels a to d. Both Λ_{Walach} and Λ_{Fogg} remain nicely matching for a while after this snapshot (see Figure 1). At 22:10 UT (Figure 2f) at 13–14 MLT the SuperDARN flows defining Λ_{Walach} lie on top of R2 currents and the boundary-defining flows agree well with the R2 boundary. Due to the boundary shape however, Λ_{Walach} and Λ_{Fogg} do not fit the R2 current boundary at the other MLTs. We note that a circular boundary would fit this interval much better.

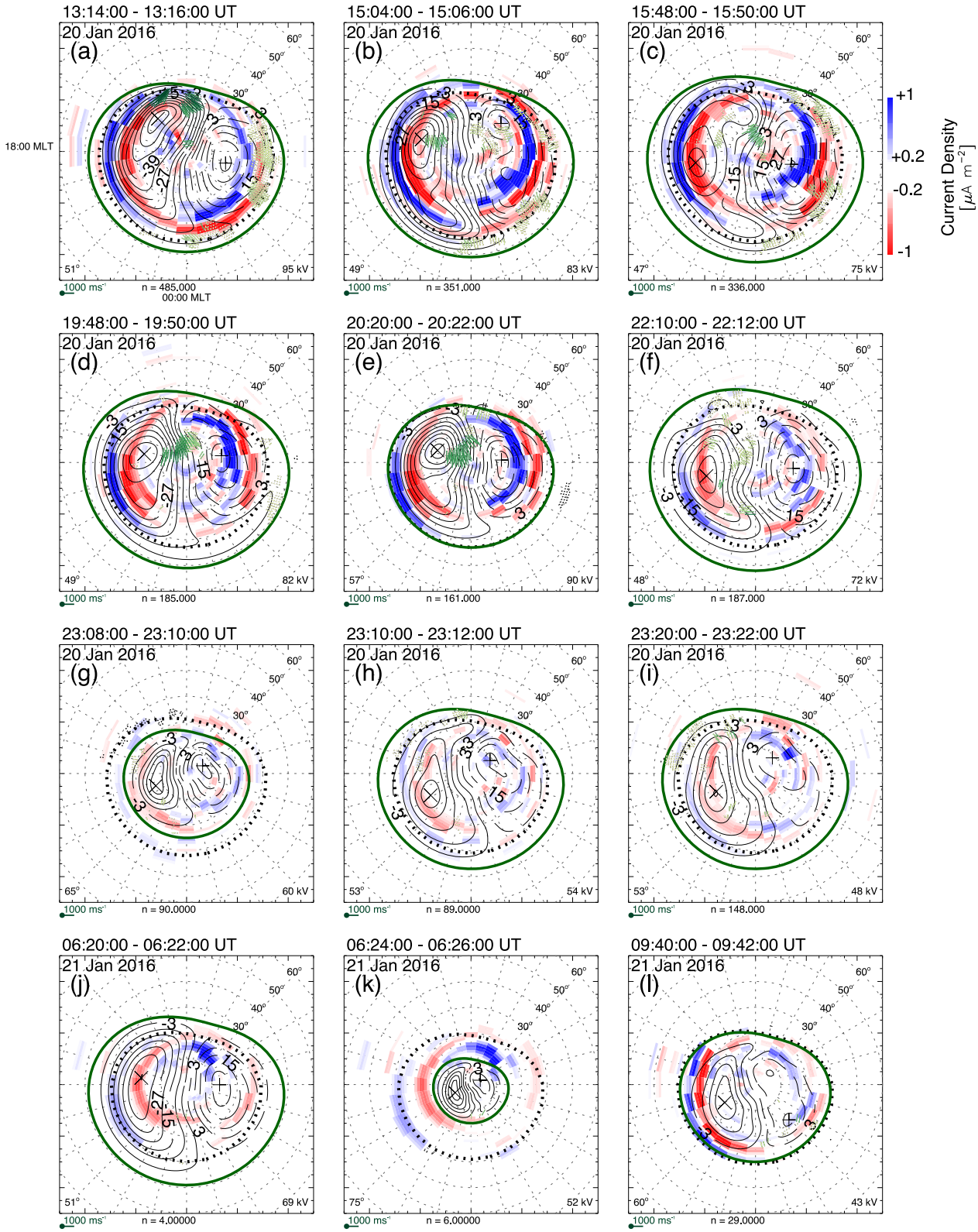

Figure 2.

Between 23:08 to 23:10 UT (Figures 2g and 2h) in the early afternoon sector, the ionospheric flows speed up to be above the 100 m/s threshold and therefore Λ_{Walach} shifts 12° in latitude. This shift is much faster than the timescales we would expect, based on our knowledge of the high-latitude system responses to solar wind driving (e.g., Coxon et al., 2019), so it is an unrealistic shift. Clearly the currents are also very weakly defined during this time, so it is generally more difficult to see any clear boundary. By 23:20 UT Figure 2i), the same early afternoon flows helps to define the convection cells nicely around R1/R2 at dusk, which matches the weak current system.

Another feature worth discussing is the sharp change seen in Λ_{Walach} at midnight just after 06:00 UT on 21 January 2016 (Figures 2j–2l). This can also be seen at day 21.25 in Figure 1a. During the slow expansion following the fast contraction, the agreement between Λ_{Walach} and the R1 FACs is remarkable in the keograms at midnight at first glance. At this time however, the AMPERE currents are weak and whilst the sharp change can be seen in the keograms, the R_F algorithm does not pick up this contraction and consequently, we do not see it in Λ_{Fogg} either. Before the expansion, at Figure 2j shows Λ_{Walach} equatorward of Λ_{Fogg} but it is clear that neither is well defined here: n is very low ($n = 4$) and the currents are weak. In Figure 2k we then see that although the currents weaken and shrink after the contraction at 06:24 UT, this is not as dramatic as the change in Λ_{Walach}, which is defined by less than 10 SuperDARN vectors and a poor quality fit. During this contraction and expansion, the Λ_{Walach} matches well with the edge of R1 at midnight, but slow flows mean that Λ_{Walach} is poorly defined, despite weak currents. As the convection pattern shrinks abruptly and then slowly expands again, the R2 is outside Λ_{Walach} for several hours. We also note that at the same time, R2 lies far equatorward of R1 at most MLTs. At 09:40 UT (Figure 2l) we show the convection pattern once it has expanded again and Λ_{Walach} is equal to Λ_{Fogg}. Despite the good match, there are still very few SuperDARN vectors ($n = 29$), but the pattern is constrained correctly by a few vectors at 1 MLT.

3.2. Event 2: 20 December 2015

Figure 3 shows the AMPERE keograms for an interval of multiple substorm onsets. In this case the boundaries expand and contract with the FACs overall, with major disagreements between the FACs and the boundaries in the northern hemisphere dawn sector. This is an interesting interval, as there is some dayside driving and Λ_{Walach} is at low latitudes for a long time (~half a day), whilst geomagnetic storm occurs, which is shown by the decrease in Sym-H in Figure 3f. During this interval we see some classic substorms in the FACs in the keograms, seen in the sawtooth-like expansions and contractions of the FACs at dawn (e.g., 354.25 DOY or 354.65 DOY and onwards) and accompanied by enhancements in AL in Figure 3f. We note that the boundaries do not always follow these expansions and contractions, which are less strongly observed in the R2 current systems than in the R1 currents. R_F does not pick up most of the expansions and contractions, which is surprising, given that they are so clear in R1.

Throughout the middle section of the event, Λ_{Walach} expands further outside the FACs than Λ_{Fogg} and R_F, as seen in Figure 3. Figure 3e shows that the difference between Λ_{Fogg} and Λ_{Walach} is positive for most of this event, which means Λ_{Walach} lies equatorward. This is due to SuperDARN registering scatter equatorward of the R2 FACs. This poses the philosophical question if the convection boundary should be the lower boundary of "polar convection" (i.e., Dungey cycle-driven) or all convection. Even flow shears produced by "sub-auroral" or "mid-latitude phenomena" should have FACs associated with them, so we argue that these should be included. The issue we are seeing with this interval is that although we measure flow shears at lower latitudes, there are only very weak FACs, suggesting either an issue with measuring FACs at these lower latitudes, possibly due to the change in magnetic field geometry. We will revisit this philosophical question in more detail in the discussion section.

Figure 4a shows a snapshot at 16:10 UT (20 December 2015). This shows a strong FAC pattern (with currents stronger than 1 μA m^{-2}) and a strong convection pattern (CPCP = 154 kV) with an extension of the dusk cell

Figure 2. Example snapshots of the polar view for Event 1: Each panel is centered on the northern magnetic pole with noon MLT pointing toward the top of the page, dusk toward the left, and midnight toward the bottom, as indicated on (a). The top left of each panel indicates the time and date of the snapshot. The colors show the AMPERE data (red = upwards current, blue = downwards current, FACs saturate at ±1 micro A m^{-2}) and the SuperDARN line-of-sight flow vectors, going from light green (slow flows) to dark green (fast flows). Vectors outside of Λ_{Walach} are shown in black. The thick green boundary shows Λ_{Walach} and the thick black dotted boundary shows Λ_{Fogg}. The equipotentials are overlaid in thin black lines. The number on the bottom left of each plot gives the latitude of Λ_{Walach} at midnight for reference and the number on the bottom right gives the polar cap potential. n shows the number of total SuperDARN vectors in each map. The latitude lines are separated by 10° and the outer co-latitudes are labeled in the top right corner of each panel. Panels a to f show panels for the different timepoints indicated in Figure 1.

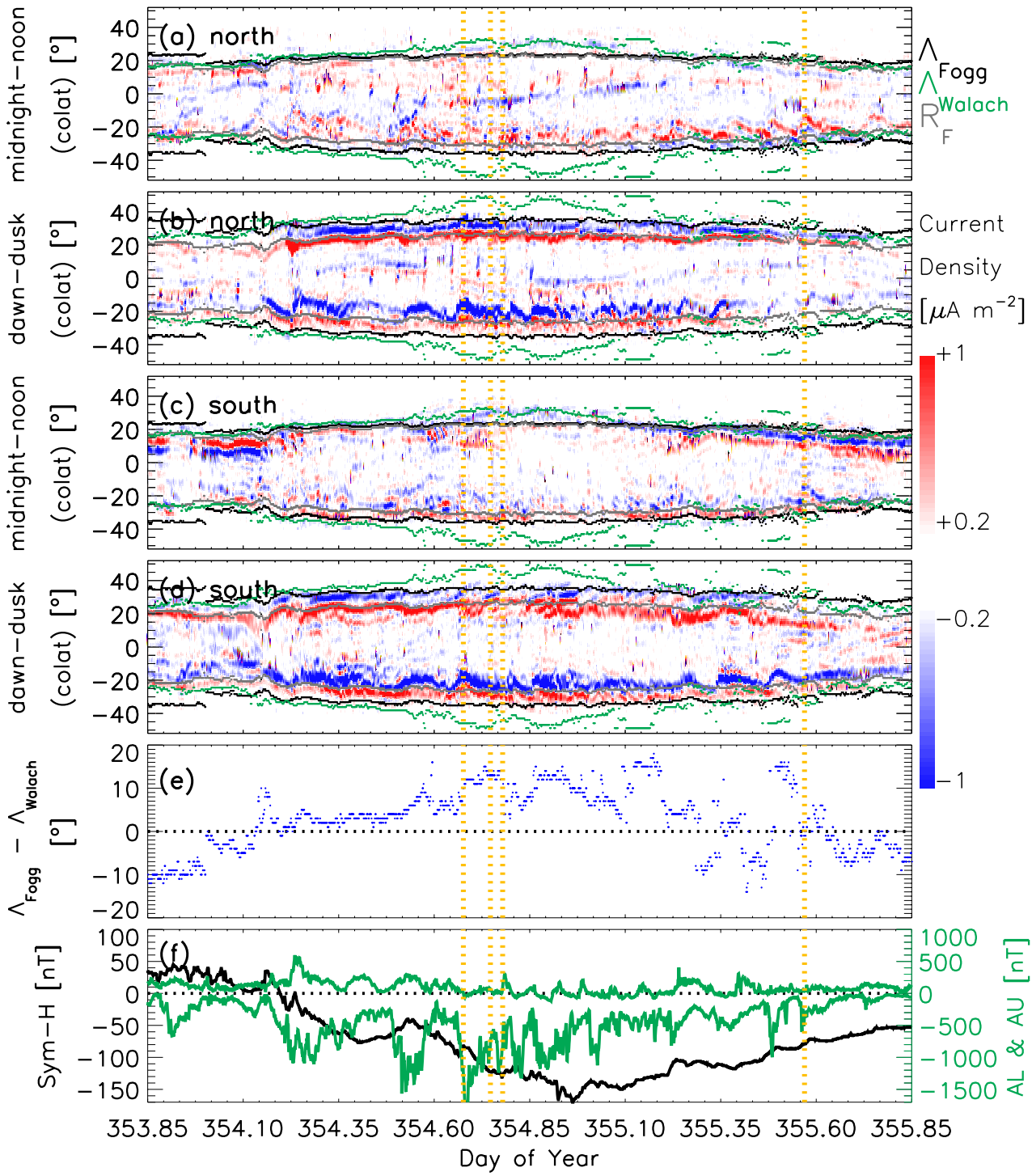

Figure 3. Six paneled plot showing keograms of the FACs and flow boundaries for 20:20 UT on 19 December 2015 to 20:20 UT on 21 December 2015 in the same format as Figure 1.

across the nightside. We also see an extension of the R1 dusk currents across midnight and merging with the R2 currents on the dawnside, which matches the extension of the convection cell, but the extension of the currents is observed at a higher latitude than Λ_{Walach}. From visual inspection, we would expect Λ_{Walach} to perhaps lie at a slightly higher latitude, but we find that this is defined by the scatter in the 11 MLT region and this moves Λ_{Walach} to lower latitudes at other MLTs due to the asymmetric shape of the boundary. This is a feature which re-emerges

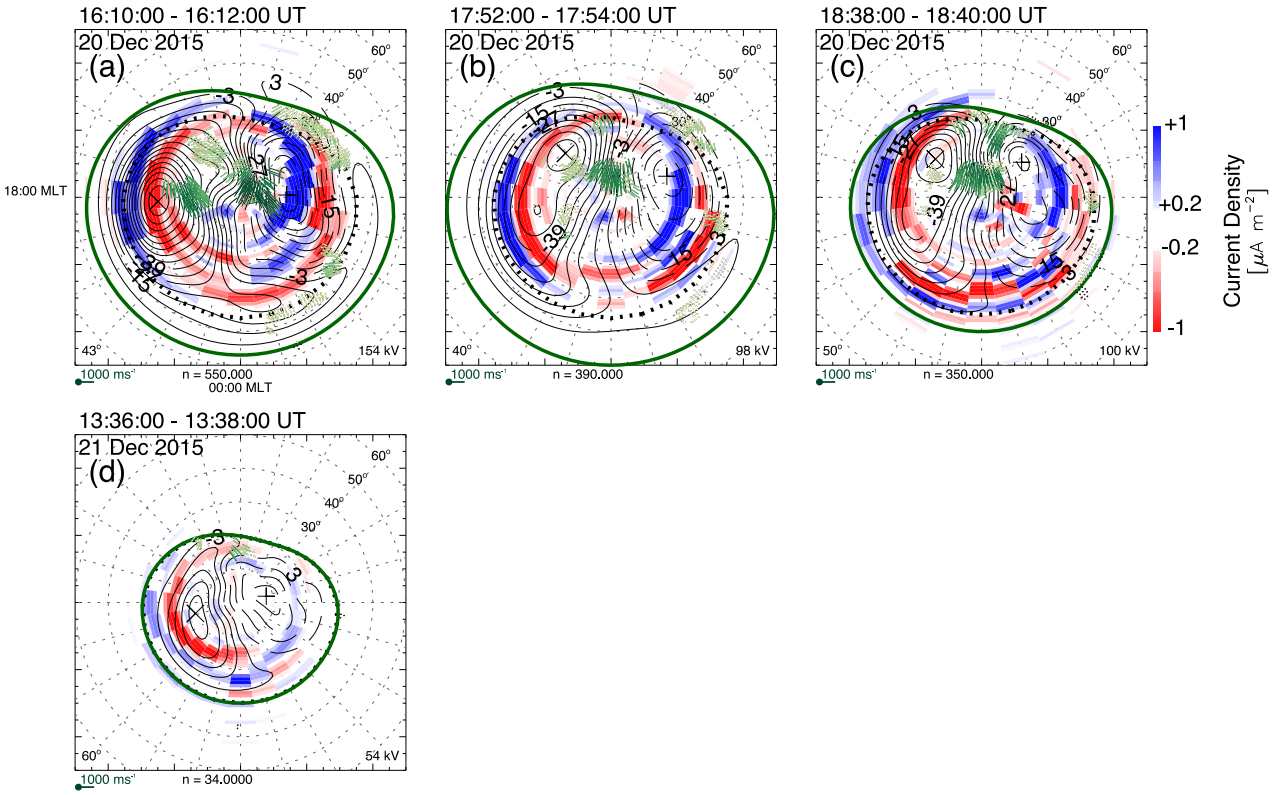

Figure 4. Example snapshots of the polar view for Event 2 in the same format as Figure 2.

throughout the interval: Dayside scatter being located at lower latitudes generally pushes Λ_{Walach} down such that it erroneously lies below the current system's locations on the nightside. This issue is exacerbated by the non-circular shape of the traditional HMB, and places a question over whether this is the correct shape to be using.

At 17:52 UT (20 December 2015, Figure 4b) we still see the extension of the dusk cell across midnight but any FACs in this region are too weak to match this flow feature. Whilst Λ_{Fogg} fits the equatorward boundary of the observed R2 currents well, it consequently lies poleward of the midnight sector convection. Λ_{Walach} is still approximately 10° equatorward. This location seems reasonable on the dayside but appears to be too far equatorward at other local times. It is evident that a circular shape for the HMB would solve this problem and fit much better here. At 18:38 UT (20 December 2015, Figure 4c) the scatter places Λ_{Walach} at 50°, which matches the R2 boundaries well, especially at dusk and midnight. On the duskside, Λ_{Fogg} lies more poleward and on top of the R2 currents (blue). At midnight Λ_{Fogg} lies just poleward of a faint upward current (red), which we judge to be equatorward of the R2 currents; the R2 currents look to be just poleward of Λ_{Fogg}. Λ_{Walach} is just equatorward of the same faint upward current. In general the midnight sector currents are quite complex at this time and we suggest they are possibly substorm-related as shown by the contractions and expansions in the FACs. There is a slight asymmetry in the currents between dusk and dawn with the dawn boundary being closer to the pole. This presents a difficult match with a boundary shape that is symmetric with respect to dusk and dawn as is the case for both boundaries shown. At 13:38 UT (21st December 2015, Figure 4d), we see the R2 currents on the duskside (blue outer circle) bifurcated, but nevertheless, Λ_{Fogg} and Λ_{Walach} are at the same latitude.

Generally in this interval, Λ_{Fogg} wraps around the currents more tightly at dusk than at dawn, and sometimes fits the extent of the current system nicely on the nightside as well. Overall, Λ_{Walach} tends to lie more equatorward, due to the dayside scatter pushing the boundary equatorward. Despite the mismatch in boundary locations, Λ_{Walach}, judged on its own, would be considered to be well-defined due to the large number of scatter points.

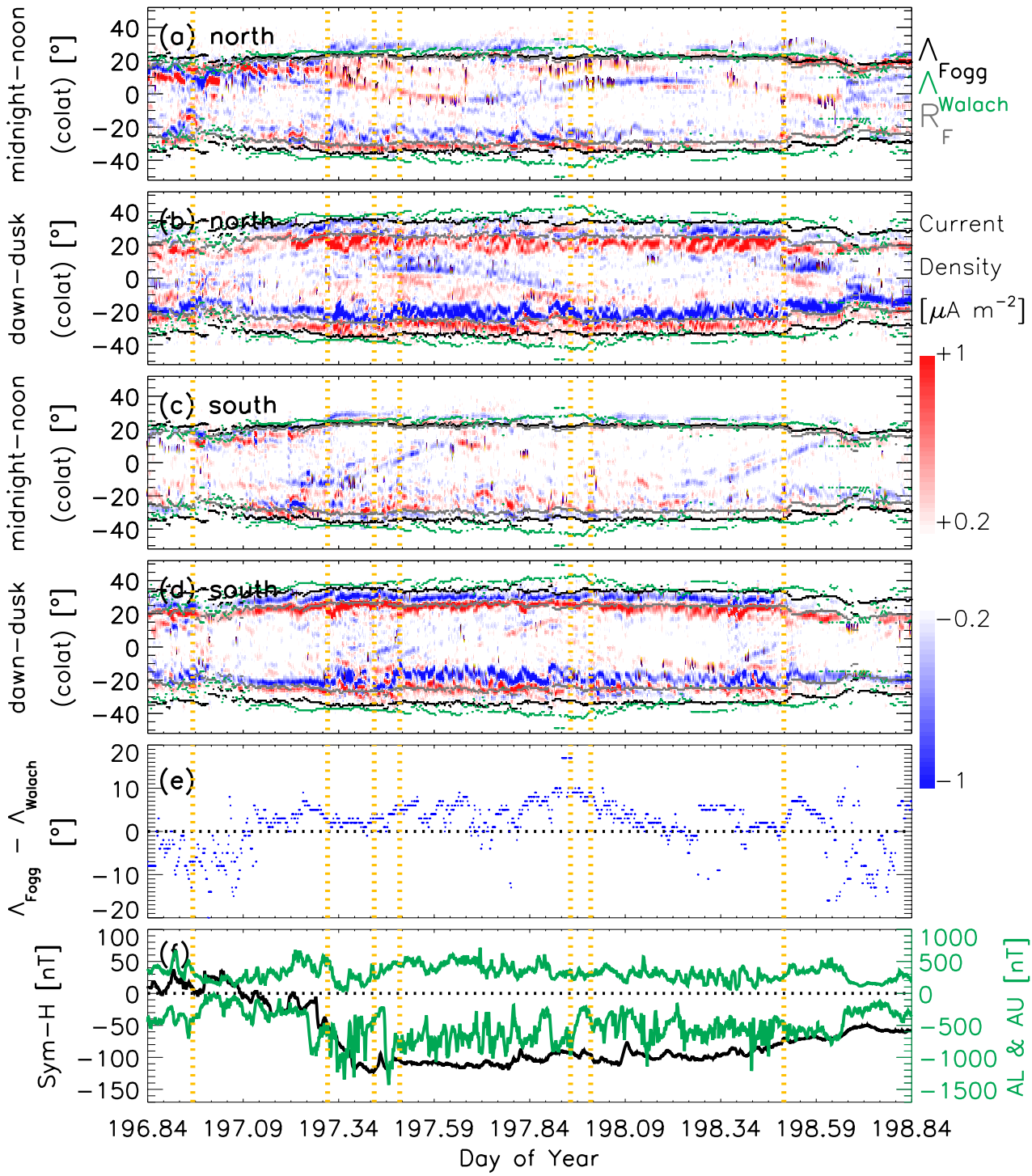

Figure 5. Six paneled plot showing keograms of the FACs and flow boundaries for 20:10 UT on 14 July 2012 to 20:10 UT on 16 July 2012 in the same format as Figures 1 and 3.

3.3. Event 3: 15 July 2012

Figures 5 and 6 are laid out in the same way as the previous plots but for event 3, which shows a strongly driven interval and a geomagnetic storm. Figure 5f shows Sym-H decreasing to ~100 nT which indicates that a geomagnetic storm is underway. AL and AU are also enhanced at the same time and we see a number of rapid

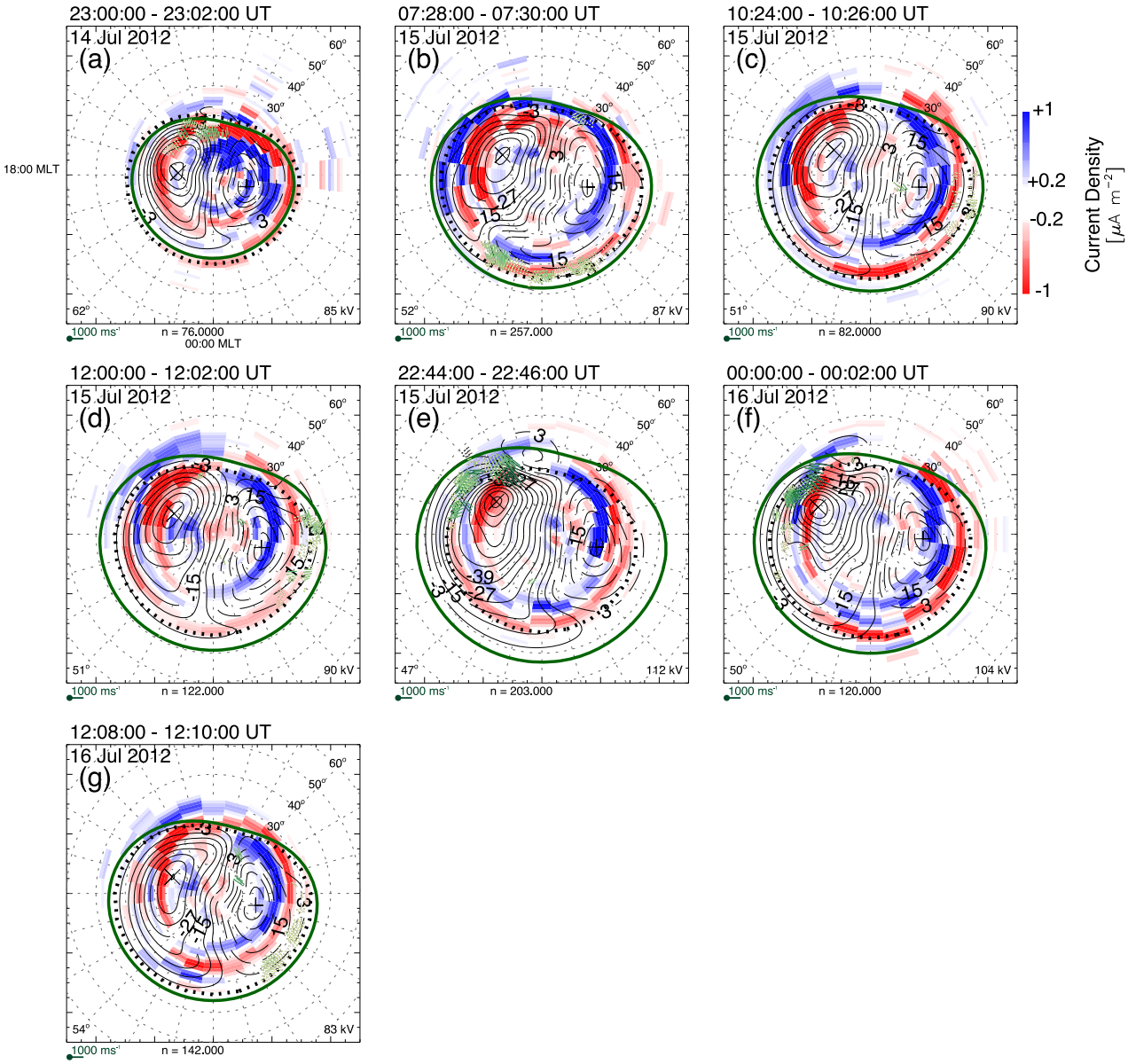

Figure 6. Example snapshots of the polar view for Event 3 in the same format as Figures 2 and 4.

enhancements in AL, which indicate a series of substorms. We see from Figure 5 that this is a very active interval with strong currents. We will return to Figure 5 after discussing a few specific polar snapshot examples from Figure 6.

Right at the beginning of the interval (14 July 2012 at 23:00 UT Figure 6a), Λ_{Walach} is poleward of Λ_{Fogg} due to insufficient vectors at lower latitudes. On 15 July 2012 after ~07:28 UT, enhanced dawn-dusk currents occur. Figure 5 shows that these dawn-dusk currents are not always symmetric around the pole, especially at dusk, where the currents are weaker. Coxon et al. (2023) also saw a systematically reduced probability of current density on the dusk side in comparison to the dawn side, which highlights an issue with fitting symmetric boundaries. Despite the weak currents, Λ_{Walach} fits the location of the currents well (see 07:28 UT Figure 6b). At 10:24 UT (Figure 6c), a bifurcation has developed on the nightside. At this point the R2 dawn currents have bifurcated and form a separate feature on the nightside (23–25 MLT). Unfortunately, we measure no SuperDARN scatter around the bifurcation, and the number of gridded SuperDARN vectors (n) is very low (82, see (Walach, Grocott, Staples, & Thomas, 2022) for how this compares to this data set in general). At 12:00 UT on 15 July 2012 (see Figures 5 and 6d)

strong R0 currents are observed but there is little co-located SuperDARN scatter observed. During this time, the R2 currents on the dayside (early afternoon sector) are very strong and located over a wide area, but there is very little SuperDARN scatter located in this area, so Λ_{Walach} is poleward of the dayside FACs. Λ_{Fogg} lies even more poleward and matches the R2 boundary well around the nightside but neither Λ_{Walach} or Λ_{Fogg} agree with the currents at 12:00 UT.

Later, at 22:44 UT (Figure 6e), Λ_{Walach} fits the afternoon sector well, being well defined by SuperDARN scatter. We also see a weak R2 bifurcation in that region (~15 MLT), which matches the location of fast scatter. The R2 at ~6 MLT also undergoes a faint bifurcation which reaches around midnight to dusk and this bifurcation persists for some time (Figure 6f). The bifurcated feature becomes the outer edge of the current system and Λ_{Fogg} matches this too. The next day, at 12:08 UT (panel g), the previous current bifurcation has disappeared but the current system is still complex. Λ_{Walach} and Λ_{Fogg} are only offset by a degree or two and both hug the current systems on the nightside. Due to the shape of the boundaries and the circular-shaped current system on the dayside, however, both boundaries do not manage to hold all the currents within.

Overall during this event, Λ_{Walach} reaches 40° but Λ_{Fogg} does not. This is for example, seen in all panels in Figure 5 at around DOY 198 (and in Figures 6e and 6f at 22:44 UT on 15 July 2012 and 00:00 UT on 16 July 2012, respectively) due to a long period of dayside driving, which drives Λ_{Walach} to low latitudes and means Λ_{Walach} is generally equatorward of Λ_{Fogg}. Here, Λ_{Walach} is fitted to scatter on the dayside, and it captures the dayside currents well as a result, but the boundary falls far outside the currents at other MLTs. The fit is particularly poor on the nightside where the currents are weaker and the early afternoon where some currents are outside Λ_{Walach} and Λ_{Fogg}. This is another example of an interval where a circular fit to the convection boundary may be more appropriate (e.g., see also Figures 2f and 4a).

In this interval we also see some instances where the FACs contract but the convection pattern (observed by SuperDARN and quantified by Λ_{Walach}) contracts more slowly. For example, at DOY ~198.5 (see 12:08 UT on 16 July 2012 in Figure 6g and region around last vertical dashed orange line in Figure 5) in the dawn/dusk currents (Figures 5b and 5d) we see an example of a quick and sharp change in the currents which is picked up by R_F and hence Λ_{Fogg}. The convection data however, and with it Λ_{Walach} responds more gradually. When we look at this in a polar view (Figure 6g), it looks like the FAC semi-circle has been shortened on the dusk side, so the dusk R2 FACs are now restricted to the noon/afternoon sector and end near dusk, as opposed to being centered on the dusk meridian. Whilst Λ_{Walach} does not match Λ_{Fogg} during this contraction at around 12:08 UT, we emphasize that this is a non-standard case as the dusk-side currents are usually centered on the dusk meridian but here they are not.

Overall, during this interval, the dawn-dusk wedges fit Λ_{Fogg} well, whereas at noon this boundary sometimes sits at higher latitudes than where the FACs terminate.

3.4. Statistical Overview

Figure 7 shows a statistical overview of the latitudinal offset between the boundaries at midnight $\delta\Lambda = \Lambda_{Fogg} - \Lambda_{Walach}$ plotted against the number of gridded SuperDARN vectors per SuperDARN map n. Each panel shows one of the three events and the data are represented as a scatter plot over a continuous probability density distribution. The vertical lines show the median (black solid), mean (black dotted) and 0° (gray dashed). In all three events, we see that on average, $\delta\Lambda > 0°$, which means Λ_{Walach} generally lies equatorward of Λ_{Fogg}.

Figure 7 also shows that the only times when $\delta\Lambda < 0°$ (such that Λ_{Fogg} is equatorward of Λ_{Walach}) occur when n is not very high (e.g., mostly less than 200). In general, when n is high, $\delta\Lambda$ tends to be greater than 0.

The probability density curves on the x- and y-axis show that a large proportion of the data (45.9%, 64.0% and 50.0%, respectively per event) is distributed in the region $0° \leq \delta\Lambda \leq 5°$ for all three events, suggesting that the two boundaries usually match well. On average, Λ_{Walach} sits ~3° equatorward of Λ_{Fogg}.

The first event has a secondary peak in $\delta\Lambda$ on the probability density curve at the top. This secondary peak lies to the left of the main peak when $\delta\Lambda \leq 10°$ and n is low (less than 100). The implication of this is that when n is low, Λ_{Walach} can be at higher latitudes than Λ_{Fogg}. These are likely times when the boundary is poorly identified by SuperDARN data.

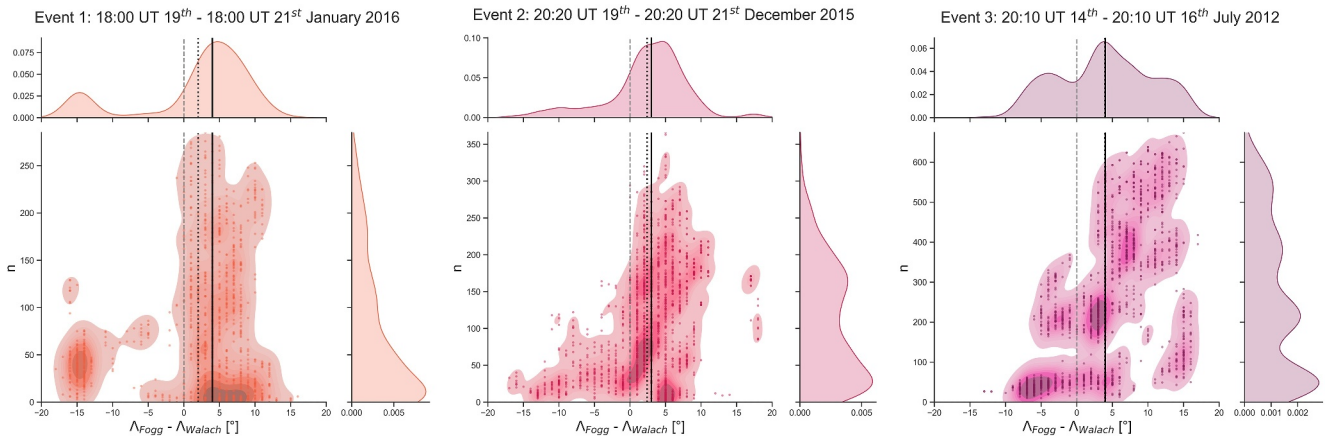

Figure 7. Three paneled figure showing the statistical distribution of the latitudinal offset between the boundaries at midnight, $\Lambda_{Fogg} - \Lambda_{Walach}$, against n for each event. The colored contours show a continuous probability density curve for each event distribution with the overlaid scatter showing the individual observations. The black solid line shows the median in $\Lambda_{Fogg} - \Lambda_{Walach}$ and the dotted black line shows the mean. The gray dashed line shows 0° difference.

We also note that the overall form of the distribution of the two right hand (pink, purple) plots are more similar to each other than the left hand plot (red). This is likely due to the fact that events 2 and 3 are more driven and have stronger geomagnetic storms whereas the first event has a weaker geomagnetic storm.

4. Discussion

The key question which we set out to answer in this study was: How reliable is the FAC boundary location at picking up the same boundary as SuperDARN for the ionospheric convection boundary? We investigated this for geomagnetic storm conditions as this causes the convection boundary to move to latitudes as low as 40° (Walach & Grocott, 2019) and latitudes below 50° were not explored by Fogg et al. (2020). In the reference frame of the neutrals, there have to be FACs at the shear of convective flows. We have found that for reasons of data quality this is not always the case. Overall, we find that Λ_{Walach} is more likely to lie equatorward of Λ_{Fogg} than the other way around. We discuss the reasons for this in the following section.

The primary reason why Λ_{Fogg} and Λ_{Walach} disagree with each other or the FAC locations is the geometry. The geometry of the standard SuperDARN boundary and the geometry of the FACs as measured by AMPERE are often in disagreement and this makes it a difficult comparison. This plays a key role in the disagreements we have uncovered. The shape of the HMB used in the SuperDARN fitting, and thus Λ_{Walach} is based on a statistical study by Heppner and Maynard (1987). Shepherd and Ruohoniemi (2000) surveyed SuperDARN data and found that the ovoid shape proposed by Heppner and Maynard (1987) was a better fit than the circle, which was used previously for the HMB-shape. This ovoid is circular along the nightside edge and indented toward the pole on the dayside. The dayside indentation matches our understanding of the magnetospheric geometry: on the dayside it is pushed into a bow-shape by the solar wind. A question that has arisen from studying these data however is: Is the SuperDARN HMB the correct shape? In some cases (e.g., Figure 4b and all panels in Figure 6), a completely circular shape would perhaps fit the AMPERE data better, but not in all cases. Another geometrical issue arises from the azimuthal asymmetries (e.g., Figure 4c at 18:38 UT Λ_{Walach} fits the AMPERE current boundary well, but on the dawnside, the AMPERE currents terminate at a higher latitude). Whilst we have not found a systematic MLT dependence of the relationship between R_F or Λ_{Fogg} and Λ_{Walach} (since this is out of the scope of this study), it is certainly clear that at different times these exist and that a circular fit for the convection boundary would therefore not always be ideal. Furthermore, Λ_{Fogg} relies on the R_F fit from Milan (2019). Due to geometrical reasons (e.g., the currents are weak or the R2 FAC regions unusually wide), R_F may be poorly constrained and therefore Λ_{Fogg} may also be poorly fitted.

Data are needed to ascertain the Λ_{Walach} placement in the standard SuperDARN fitting but the primary limitation is the coverage. For example, in many cases there is little backscatter observed equatorward of the dayside boundary, which makes this identification difficult. One way to use data for boundary selection is to use AMPERE data as was done for Λ_{Fogg}. This comes with its own challenges: As we have shown, sometimes the data

do not agree and whilst the fitted AMPERE boundaries (R_F) are circular, the morphologies of the FACs are not necessarily circular (or fitting to the functional SuperDARN HMB form) either. We have also seen a number of cases where the convection pattern expands or contracts and these boundary movements are out of step with each other. We have seen examples in every one of the three events, where the AMPERE pattern contracts and the contraction in the SuperDARN convection pattern is delayed. This suggests there are some feedback effects in the ionosphere, which could be a sign of a delay in the communication times between currents and convection or a sign of sensitivity issues with the temporal/spatial cadence of AMPERE. Expansions are mostly in time with each other, but there are also examples when the AMPERE pattern expands very rapidly and this is not reflected in the SuperDARN pattern. Most likely, changes reflected in the AMPERE FACs or SuperDARN convection are due to changes in one local time which affect the global fitting. For example, we see such changes from Figure 2d to 2e), where the SuperDARN measurements at ∼4 MLT are at first included in the convection pattern but then fall below the Λ_{Walach} boundary due to slow scatter on the dayside fixing Λ_{Walach} in Figure 2.

Whilst the main limitation of the SuperDARN-method of determining the convection boundary (Λ_{Walach}) is data availability, the Fogg-method of determining the boundary (Λ_{Fogg}) brings its own challenges. We find that when the currents are very weak (e.g. at the beginning of event 1), the R_F boundary cannot be found, whereas the SuperDARN data can find and constrain the convection boundary. In this case, one could apply the Fogg-method to averaged maps of AMPERE data but this is still likely to yield no boundary when currents are weak. Instead, one could use the SuperDARN boundary when no boundary can be derived from AMPERE.

Imber et al. (2013b) previously studied how the HMB moves with the auroral oval. They found that by smoothing the HMB latitude across time, and comparing this to the brightest part of the auroral oval, the HMB lies just a few degrees equatorward of the auroral oval. Whilst this is reflected by some of our results, we caution against such a generalization: Our data clearly shows that there is complexity in the data that cannot be summarized by a simple relationship. Furthermore, Imber et al. (2013b) used data from 2000 to 2002, but during this time, the SuperDARN fitting was not able to place the HMB below 50° geomagnetic latitude due to limited radar coverage (Walach & Grocott, 2019), so it is not a useful comparison for our study which exclusively has focused on geomagnetic storms. To add further context to the equivalence of the auroral oval and FACs, we point the reader to Carter et al. (2016) who showed that the statistical distribution of FACs is not necessarily a good indicator of auroral location.

According to the diagram in Figure 2 of Milan et al. (2017) (see also e.g. Cowley, 2000), convection happens between R1 and R2 FACs. This assumes that the neutral atmosphere is stationary in reference to the electric fields. We observe convection on the R2 FACs or, when current bifurcations are present, on a R2 bifurcation, or indeed between the R2 and the bifurcation. Often, the return flows also occur on the R1 FACs, which also does not match the cartoon from Milan et al. (2017) and therefore our understanding of the electrodynamics. We put forward two reasons for this. On a statistical level, the Λ_{Fogg} and Λ_{Walach} compare well, but as we have shown, over just three short events, there can be a large amount of discrepancy (up to 20°). This discrepancy tends to be larger when the number of backscatter echoes in the SuperDARN maps is lower, suggesting that this is primarily due to uncertainty in identifying Λ_{Walach} when data coverage is lower. We have shown that, on average, Λ_{Walach} sits at lower latitudes than Λ_{Fogg} with a systematic offset of ∼3°. This compares to the root mean square error found by Fogg et al. (2020) (2.75°), who correlated the HMB at midnight with R_F. We also find, however, that the latitudinal difference between the two boundaries is not always systematic and it is not possible to choose which boundary fitting (Λ_{Fogg} or Λ_{Walach}) is best overall. This also shows that there is a deeper gap in our understanding which goes beyond the geometries of the data fitting and the magnetosphere-ionosphere system: If the AMPERE and SuperDARN data do not match in their dynamic signatures, there is something missing. This is most likely related to the data processing (both data sets undergo a number of fitting steps), it could be a physical decoupling between the altitude at which the data are sampled (e.g., SuperDARN and AMPERE are obtained at ∼300 km and ∼780 km, respectively). A key assumption that is often made is that the conductivity is uniform. Since the conductivity relates ionospheric vorticity and the field-aligned current strength, it is also likely that uniform conductivity is a poor assumption. In any case, it is a gap in our understanding.

No data processing technique is perfect. Missing SuperDARN backscatter often means the maps are constructed by extrapolating the background model and Λ_{Walach} from MLT sectors with data coverage to MLT sectors with no scatter. This has the benefit that maps can be constructed without fully global data coverage but it does also mean that care has to be taken with interpreting the maps. Currently, there is no established way of assessing convection map quality beyond the number of vectors and this is something that needs to be established (e.g., see discussion

by Walach, Grocott, Staples, & Thomas, 2022). There could be errors in the geolocation of SuperDARN scatter, which could put velocity shears into the wrong place but we have minimised this in our data processing technique as described in Walach, Grocott, Staples, and Thomas (2022).

Indeed, there is currently no way to verify "best" fit or latitude position for the HMB for any given map, independent of SuperDARN scatter availability. Fogg et al. (2020) sought to overcome dependence on scatter availability by using an independent data source (AMPERE) to define the equatorward boundary of convection. In this study we show some agreement, and some disagreement between boundaries using the method of Fogg et al. (2020) and the traditionally determined HMB. Along with our observations on the shape of the HMB, and uncertainty in the types of flows, this generates important questions for the community: how best can we define the equatorward edge of the convection pattern, and what types of flows should we include in this convection pattern? For example, should it only include Dungey-driven convection or also sub-auroral phenomena?

The ionosphere does not always truly become stationary at latitudes below Λ_{Walach}, even in the rest frame of the neutrals. There are published results with SuperDARN indicating that, in addition to SAPS, reduced, but still finite, flows continue below that boundary (Maimaiti et al., 2019). In whole atmospheric modelling communities, however, and even magnetospheric physics, the electric fields generated by the Dungey-driven convection pattern and lower latitudes are thought of as two separate "fields". It is however not conducive to think of these as separate since all shear flows should be associated with FACs, unless the magnetosphere-ionosphere are no longer coupled. Furthermore, the SuperDARN fitting technique was designed to encompass all flows since they all have to be incompressible and must map to plasma convection in the magnetosphere, which is communicated by FACs. Due to limitations in radar coverage, SuperDARN background models did traditionally not include mid-latitude or sub-auroral phenomena, but it is crucial that this is advanced, since all convection should be captured with the convection maps. Especially when we discuss features such as bifurcations (Sangha et al., 2020) and SAPS (e.g., Foster & Vo, 2002; Kunduri et al., 2018), which are often observed together (Sangha et al., 2020), and originate in the return flow part of the traditional two-cell pattern (Sangha et al., 2020), so they are an integral part to convection. Sangha et al. (2020) showed that this is a phenomenon that commonly occurs during substorms.

Whilst it might be a challenge, we must incorporate SAPS and bifurcations in the convection maps and improve the fitting techniques to be able to do so without compromising overall quality. Λ_{Walach} is more likely to be influenced by mid-to low-latitude phenomena, but as we have shown, current bifurcations occur frequently and should not be dismissed as a mere outlier. The biggest question surrounding these features is where in the magnetosphere the FACs associated with these flows close and to answer this effectively, we must be able to map the bifurcations and SAPS alongside all other currents and flows.

We have alluded to the fact that the equatorward extent of the convection and the FACs can be decoupled. In summary, we have discussed the uncertainties around conductivity, geometry, data processing methods, time-varying phenomena such as SAPS and possibly inductive effects which can offset these boundaries. We further add that if the response times of the convection and FACs are different, the data may appear decoupled due to the sampling rate, but the electrodynamics have to be consistent. We conclude that conductivity gradients would be the most likely factor in generating an observed inconsistency between FACs and the convection: it is possible that FACs would preferentially close at higher latitudes through regions of high conductivity (e.g., in the auroral regions), whilst convection can continue at lower latitudes in regions where the currents do not propagate as easily.

5. Summary

In this article we have presented three case studies to observe and compare the SuperDARN-derived HMB (Λ_{Walach}) and the equivalent boundary of the FACs (Λ_{Fogg}). The purpose of this was two-fold: First, we compare Λ_{Walach} to a newer method from Fogg et al. (2020). The Fogg et al. (2020) method used a statistical AMPERE database to develop an empirical model for the FAC boundary, whereas Λ_{Walach} chooses the boundary based on the lowest latitude at which the flow vectors approach 0 m/s. Second, the purpose of this study was to compare the boundaries to the FACs themselves. This is not necessarily the same as Λ_{Fogg}, as Λ_{Fogg} relies on a fit between the R1 and R2 currents. With our case studies, we have established how well the different boundaries match each other, but also, and perhaps more crucially, find instances when they do not match. These are important and novel results as, theoretically, the boundaries should match (e.g., Milan et al., 2017).

Overall, our observations show the following.

- Agreement between Λ_{Fogg}, the FAC-derived boundary, and Λ_{Walach}, the flow-derived boundary is likely to be best when the SuperDARN data coverage is high.
- On average, Λ_{Walach} is $\sim 3°$ equatorward of Λ_{Fogg}.
- Poor agreement between the Λ_{Fogg} and Λ_{Walach} comes from either: (a) Not enough scatter at different latitudes and MLT, which leads to poor fitting; (b) Deformations such as bifurcations/asymmetries in the FAC pattern.
- During geomagnetically active times, a circular HMB may present a better fit.
- Instances where Λ_{Walach} and Λ_{Fogg} match each other on the dayside but not on the nightside (and vice versa) and fit well at dusk but not dawn (and vice versa), happen often. This is mostly due to late morning scatter which has defined Λ_{Walach}, and is colocated with the currents. This does however lead to Λ_{Walach} being at much lower latitude on the nightside than Λ_{Fogg} and is one of the main reasons for poor agreement on the nightside.
- Most often Λ_{Walach} fits the Λ_{Fogg} best in the dusk/afternoon sector.
- Sometimes Λ_{Walach} sits at lower latitudes than the currents because the return flows are observed below the R2 FACS or the flows sit on a FAC bifurcation.
- If there is an offset between Λ_{Walach} and FAC pattern, it is around 3–5°; and in cases where this occurs, the convection cells fit well around the FACs, but the return flow region stretches to lower latitudes.
- Λ_{Fogg} does not always follow the expansions/contractions in the FACs. Λ_{Fogg} relies on the R1/R2 boundary being fitted well and this is not always the case for expansions/contractions of the current system.
- Most of the sharp contractions in the current systems are not shown in Λ_{Walach}. This is either because the scatter disappears (and it is therefore not measurable) or Λ_{Walach} is more slow to respond, which may be due to inertial coupling between the neutrals and ions at a lower altitude to AMPERE, and AMPERE is therefore not sensitive enough to pick up.

It is clear that no data set is perfect and this is important to discuss and keep in mind. A crucial factor is the data processing. We have shown that the shape used for the fitting is not always appropriate. Sometimes, a more asymmetric boundary would be beneficial and often times, a circular boundary would match the AMPERE data better. Unfortunately, without better SuperDARN coverage at mid-latitudes and a way to assess the quality of convection maps, trust in the boundary is difficult to establish. This study has however also made clear that there are times when Λ_{Walach} and Λ_{Fogg} do not match, despite sufficient SuperDARN scatter to be confident of reliable boundary placement. As such, our physical understanding of these cases is lacking. A good example of this is the observation that the FAC systems sometimes contract much quicker than the SuperDARN boundaries. As this happens on timescales that are several times longer than the Alfvén response times, we theorize that this is due to the inertia of the neutral atmosphere affecting the ionosphere and AMPERE measures variations in the magnetic field, which do not always reflect changes in the ionosphere. This is a phenomenon that is poorly understood, especially since we observe this at the mid-latitudes, where SuperDARN observations have only been available since 2012. Furthermore, prior to Walach and Grocott (2019) and SuperDARN Data Analysis Working Group, Thomas, Ponomarenko, Billett, et al. (2018), all SuperDARN convection maps had a hard-coded 50° latitudinal limit for the convection boundary, which has previously hindered our ability to study expanded convection patterns in detail.

We have discussed challenges in comparing the AMPERE and SuperDARN data sets, which have highlighted that open questions remain regarding convection mapping. In summary, these open questions are.

- What makes a good quality map? Currently, there is no established criteria to evaluate quality due to a lack of comparable data sets (see discussion in Walach, Grocott, Staples, & Thomas, 2022).
- What is the correct shape of the HMB? We have shown here that sometimes a circular boundary may be more appropriate than what is currently used.
- How many vectors are enough to make a map and what should be used as a threshold for the HMB? We note here that Thomas and Shepherd (2018) for example, used a more stringent criteria of 25 vectors with velocities greater than 150 m/s to determine the HMB location but this is not feasible for usual convection mapping due to the vector coverage.
- Can we map convection in a coherent way which includes convection-related sub-auroral phenomena, such as SAPs?

Data Availability Statement

All SuperDARN and AMPERE data is openly available. Access to the SuperDARN database is available via the British Antarctic Survey and the University of Saskatchewan. The Radar Software Toolkit (RST) to process the SuperDARN data can be downloaded from https://github.com/SuperDARN/rst (SuperDARN Data Analysis Working Group, Thomas, Ponomarenko, Billett, et al., 2018). We thank the AMPERE team and the AMPERE Science Center for providing the Iridium derived data products. All AMPERE data are available online (via https://ampere.jhuapl.edu). The SuperDARN convection maps used in this study, as well as the polar plots of SuperDARN and AMPERE and the Λ_{Fogg} and Λ_{Walach} values are available in Walach and Fogg (2024b). R_F boundaries are available online (from https://doi.org/10.25392/leicester.data.11294861.v1). We acknowledge use of NASA/GSFC's Space Physics Data Facility's CDAWeb service, and OMNI data. In the SI we show the solar wind data and geomagnetic indices at 1-min resolution, which are extracted from the OMNI data (King & Papitashvili, 2005). The geomagnetic indices are also shown in Figures 1, 3 and 5. In the SI we also show Φ_D, the dayside reconnection rate, which is derived from the OMNI data using the equation derived by Milan et al. (2012).

Acknowledgments

This work is dedicated to the memory of Kathryn McWilliams who suddenly passed away during the reviewing process of this manuscript. The authors acknowledge the use of SuperDARN data. SuperDARN is a collection of radars funded by national scientific funding agencies of Australia, Canada, China, France, Italy, Japan, Norway, South Africa, United Kingdom, and United States of America, and we thank the international PI team for providing the data. The authors acknowledge access to the SuperDARN database via the British Antarctic Survey. Other SuperDARN data mirrors are available via the Virginia Tech SuperDARN group and the University of Saskatchewan. The Radar Software Toolkit (RST) to process the SuperDARN data can be downloaded from https://github.com/SuperDARN/rst (SuperDARN Data Analysis Working Group, Thomas, Ponomarenko, Billett, et al., 2018). MTW acknowledges the use of the Lancaster University High-End Computing Cluster (HEC), which has greatly facilitated The SuperDARN data processing, and Mike Pacey's HEC support. The authors thank the SuperDARN PIs for their continued work in making SuperDARN data available and the SuperDARN Data Analysis Working Group in their ongoing efforts to improve the software quality and accessibility. Support for AMPERE has been provided under NSF award AGS-2002574. We thank the AMPERE team and the AMPERE Science Data Center for providing data products derived from the Iridium Communications constellation, enabled by support from the National Science Foundation. We thank King, Papitashvili and NASA for the provision of the OMNI data set through the CDAWeb service and acknowledge the use of this for the information shown in the SI. MTW gratefullly acknowledge funding through the UKRI STFC Ernest Rutherford fellowship (grant ST/X003663/1). MTW and AG gratefully acknowledge the funding from the UKRI Natural Environment Funding Council (grants NE/T000937/1 and NE/P001556/1 and NE/V00283X/1). ARF was supported by an STFC studentship and Irish Research Council Government of Ireland Postdoctoral Fellowship (grant GOIPD/2022/782). ML and SEM acknowledge support from the UK Science and Technology Facilities Council (grant ST/W00089X/1). JCC acknowledges support from the UKRI STFC Ernest Rutherford Fellowship (grant ST/V004883/1). SKV and BJA were supported by NSF Award AGS-2002574. For the purpose of open access, the authors have applied a Creative Commons Attribution (CC BY) licence to any Author Accepted Manuscript version arising.

References

Anderson, B. J., Angappan, R., Barik, A., Vines, S. K., Stanley, S., Bernasconi, P. N., et al. (2021). Iridium communications satellite constellation data for study of earth's magnetic field. *Geochemistry, Geophysics, Geosystems*, *22*(8), e2020GC009515. https://doi.org/10.1029/2020GC009515

Anderson, B. J., Korth, H., Waters, C. L., Green, D. L., Merkin, V. G., Barnes, R. J., & Dyrud, L. P. (2014). Development of large-scale birkeland currents determined from the active magnetosphere and planetary electrodynamics response experiment. *Geophysical Research Letters*, *41*(9), 3017–3025. https://doi.org/10.1002/2014GL059941

Anderson, B. J., Takahashi, K., & Toth, B. A. (2000). Sensing global birkeland currents with iridium® engineering magnetometer data. *Geophysical Research Letters*, *27*(24), 4045–4048. https://doi.org/10.1029/2000GL000094

Birkeland, K. R. (1908). The Norwegian Aurora Polaris Expedition 1902-1903, vol. 1, first section, Part I, on the cause of magnetic storms and the origin of terrestrial magnetism. *Christiania: H. Aschehoug & Co*, 1–413.

Birkeland, K. R. (1913). The Norwegian Aurora Polaris Expedition 1902-1903, vol. 1, second section, Part II, Polar magnetic phenomena and terrella experiments. *Christiania: H. Aschehoug & Co*, 413–994.

Bristow, W. A., & Jensen, P. (2007). A superposed epoch study of SuperDARN convection observations during substorms. *Journal of Geophysical Research*, *112*(A06232), 1–14. https://doi.org/10.1029/2006JA012049

Bristow, W. A., Otto, A., & Lummerzheim, D. (2001). Substorm convection patterns observed by the super dual auroral radar network. *Journal of Geophysical Research*, *106*(A11), 24593–24609. https://doi.org/10.1029/2001JA000117

Bristow, W. A., Sofko, G. J., Stenbaek-Nielsen, H. C., Wei, S., Lummerzheim, D., & Otto, A. (2003). Detailed analysis of substorm observations using superdarn, uvi, ground-based magnetometers, and all-sky imagers. *Journal of Geophysical Research*, *108*(A3), 1–14. https://doi.org/10.1029/2002JA009242

Carter, J., Milan, S., Coxon, J., Walach, M.-T., & Anderson, B. (2016). Average field-aligned current configuration parameterized by solar wind conditions. *Journal of Geophysical Research A: Space Physics*, *121*(2), 1294–1307. https://doi.org/10.1002/2015JA021567

Chisham, G., Lester, M., Milan, S. E., Freeman, M. P., Bristow, W. a., Grocott, a., et al. (2007). A decade of the super dual auroral radar network (SuperDARN): Scientific achievements, new techniques and future directions. *Surveys in Geophysics*, *28*(1), 33–109. https://doi.org/10.1007/s10712-007-9017-8

Clausen, L. B. N., H. Baker, J. B., Ruohoniemi, J. M., Milan, S. E., Coxon, J. C., Wing, S., et al. (2013). Temporal and spatial dynamics of the regions 1 and 2 Birkeland currents during substorms. *Journal of Geophysical Research: Space Physics*, *118*(6), 3007–3016. https://doi.org/10.1002/jgra.50288

Cowley, S. W. H. (2000). Magnetosphere-ionosphere interactions: A tutorial review. In *Magnetospheric current systems* (pp. 91–106). American Geophysical Union (AGU). https://doi.org/10.1029/GM118p0091

Cowley, S. W. H., & Lockwood, M. (1992). Excitation and decay of solar wind-driven flows in the magnetosphere-ionophere system. *Annales Geophysicae*, *10*, 103–115.

Coxon, J. C., Chisham, G., Freeman, M. P., Forsyth, C., Walach, M.-T., Murphy, K. R., et al. (2023). Extreme birkeland currents are more likely during geomagnetic storms on the dayside of the earth. *Journal of Geophysical Research: Space Physics*, *128*(12), e2023JA031946. https://doi.org/10.1029/2023JA031946

Coxon, J. C., Milan, S. E., & Anderson, B. J. (2018). A review of birkeland current research using ampere. In *Electric currents in geospace and beyond* (pp. 257–278). American Geophysical Union (AGU). https://doi.org/10.1002/9781119324522.ch16

Coxon, J. C., Milan, S. E., Clausen, L. B. N., Anderson, B. J., & Korth, H. (2014). A superposed epoch analysis of the regions 1 and 2 Birkeland currents observed by AMPERE during substorms. *Journal of Geophysical Research: Space Physics*, *119*(12), 1–13. https://doi.org/10.1002/2014JA020500

Coxon, J. C., Rae, I. J., Forsyth, C., Jackman, C. M., Fear, R. C., & Anderson, B. J. (2017). Birkeland currents during substorms: Statistical evidence for intensification of regions 1 and 2 currents after onset and a localized signature of auroral dimming. *Journal of Geophysical Research: Space Physics*, *122*(6), 6455–6468. https://doi.org/10.1002/2017JA023967

Coxon, J. C., Shore, R. M., Freeman, M. P., Fear, R. C., Browett, S. D., Smith, A. W., et al. (2019). Timescales of birkeland currents driven by the imf. *Geophysical Research Letters*, *46*(14), 7893–7901. https://doi.org/10.1029/2018GL081658

Davis, T. N., & Sugiura, M. (1966). Auroral electrojet activity index AE and its universal time variations. *Journal of Geophysical Research*, *71*(3), 785–801. https://doi.org/10.1029/JZ071i003p00785

Dungey, J. W. (1961). Interplanetary magnetic field and the auroral zones. *Physical Review Letters*, *6*(2), 47–48. https://doi.org/10.1103/PhysRevLett.6.47

Dungey, J. W. (1963). Interactions of solar plasma with the geomagnetic field. *Planetary and Space Science*, *10*, 223–237. https://doi.org/10.1016/0032-0633(63)90020-5

Elsden, T., Yeoman, T. K., Wharton, S. J., Rae, I. J., Sandhu, J. K., Walach, M.-T., et al. (2022). Modeling the varying location of field line resonances during geomagnetic storms. *Journal of Geophysical Research: Space Physics*, *127*(1), e2021JA029804. https://doi.org/10.1029/2021JA029804

Fogg, A. R. (2020). SuperDARN Heppner-Maynard boundaries. https://doi.org/10.25392/leicester.data.11854713.v1

Fogg, A. R., Lester, M., Yeoman, T. K., Burrell, A. G., Imber, S. M., Milan, S. E., et al. (2020). An improved estimation of SuperDARN Heppner-Maynard boundaries using AMPERE data. *Journal of Geophysical Research: Space Physics*, *125*(5), e2019JA027218. https://doi.org/10.1029/2019JA027218

Foster, J. C., & Vo, H. B. (2002). Average characteristics and activity dependence of the subauroral polarization stream. *Journal of Geophysical Research*, *107*(A12), 1475. https://doi.org/10.1029/2002JA009409

Gonzalez, W. D., Joselyn, J. A., Kamide, Y., Kroehl, H. W., Rostoker, G., Tsurutani, B. T., & Vasyliunas, V. M. (1994). What is a geomagnetic storm? *Journal of Geophysical Research*, *99*(A4), 5771–5792. https://doi.org/10.1029/93JA02867

Greenwald, R. A., Baker, K. B., Dudeney, J. R., Pinnock, M., Jones, T. B., Thomas, E. C., et al. (1995). Darn/Superdarn; A global view of the dynamics of high-latitude convection. *Space Science Reviews*, *71*(1–4), 761–796. https://doi.org/10.1007/BF00751350

Heppner, J. P. (1972). Electric field variations during substorms: Ogo-6 measurements. *Planetary and Space Science*, *20*(9), 1475–1498. https://doi.org/10.1016/0032-0633(72)90052-9

Heppner, J. P., & Maynard, N. C. (1987). Empirical high-latitude electric field models. *Journal of Geophysical Research*, *92*(A5), 4467–4489. https://doi.org/10.1029/JA092iA05p04467

Iijima, T., & Potemra, T. A. (1978). Large-scale characteristics of field-aligned currents associated with substorms. *Journal of Geophysical Research*, *83*(A2), 599–615. https://doi.org/10.1029/JA083iA02p00599

Imber, S. M., Milan, S. E., & Lester, M. (2013a). The Heppner-Maynard Boundary measured by SuperDARN as a proxy for the latitude of the auroral oval. *Journal of Geophysical Research: Space Physics*, *118*(2), 685–697. https://doi.org/10.1029/2012JA018222

Imber, S. M., Milan, S. E., & Lester, M. (2013b). Solar cycle variations in polar cap area measured by the superDARN radars. *Journal of Geophysical Research: Space Physics*, *118*(10), 6188–6196. https://doi.org/10.1002/jgra.50509

Iyemori, T. (1990). Storm-time magnetospheric currents inferred from mid-latitude geomagnetic field variations. *Journal of Geomagnetism and Geoelectricity*, *42*(11), 1249–1265. https://doi.org/10.5636/jgg.42.1249

King, J. H., & Papitashvili, N. E. (2005). Solar wind spatial scales in and comparisons of hourly Wind and ACE plasma and magnetic field data. *Journal of Geophysical Research*, *110*(A2), 1–9. https://doi.org/10.1029/2004JA010649

Kunduri, B. S. R., Baker, J. B. H., Ruohoniemi, J. M., Nishitani, N., Oksavik, K., Erickson, P. J., et al. (2018). A new empirical model of the subauroral polarization stream. *J. Geophys. Res-Space Phys.*, *123*(9), 7342–7357. https://doi.org/10.1029/2018JA025690

Lester, M. (2008). SuperDARN: An example of a network approach to geospace science in the twenty-first century. *Journal of Atmospheric and Solar-Terrestrial Physics*, *70*(18), 2309–2323. https://doi.org/10.1016/j.jastp.2008.08.003

Lockwood, M. (1991). On flow reversal boundaries and transpolar voltage in average models of high-latitude convection. *Planetary and Space Science*, *39*(3), 397–409. https://doi.org/10.1016/0032-0633(91)90002-r

Maimaiti, M., Baker, J. B. H., Ruohoniemi, J. M., & Kunduri, B. (2019). Morphology of nightside subauroral ionospheric convection: Monthly, seasonal, kp, and imf dependencies. *Journal of Geophysical Research: Space Physics*, *124*(6), 4608–4626. https://doi.org/10.1029/2018JA026268

McWilliams, K. A., Yeoman, T. K., Sigwarth, J. B., Frank, L. A., & Brittnacher, M. (2001). The dayside ultraviolet aurora and convection responses to a southward turning of the interplanetary magnetic field. *Annales Geophysicae*, *19*(7), 707–721. https://doi.org/10.5194/angeo-19-707-2001

Milan, S. E. (2019). AMPERE R1/R2 FAC radii. https://doi.org/10.25392/leicester.data.11294861.v1

Milan, S. E., Carter, J. A., Korth, H., & Anderson, B. J. (2015). Principal component analysis of birkeland currents determined by the active magnetosphere and planetary electrodynamics response experiment. *Journal of Geophysical Research: Space Physics*, *120*(12), 10415–10424. https://doi.org/10.1002/2015JA021680

Milan, S. E., Clausen, L., Coxon, J., Carter, J., Walach, M.-T., Laundal, K., et al. (2017). Overview of solar wind-magnetosphere-ionosphere-atmosphere coupling and the generation of magnetospheric currents. *Space Science Reviews*, *206*(1–4), 547–573. https://doi.org/10.1007/s11214-017-0333-0

Milan, S. E., Gosling, J. S., & Hubert, B. (2012). Relationship between interplanetary parameters and the magnetopause reconnection rate quantified from observations of the expanding polar cap. *Journal of Geophysical Research*, *117*(A3), A03226. https://doi.org/10.1029/2011JA017082

Milan, S. E., Sato, N., Ejiri, M., & Moen, J. (2001). Auroral forms and the field-aligned current structure associated with field line resonances. *Journal of Geophysical Research*, *106*(A11), 25825–25833. https://doi.org/10.1029/2001JA900077

Nishitani, N., Ruohoniemi, J. M., Lester, M., Baker, J. B. H., Koustov, A. V., Shepherd, S. G., et al. (2019). Review of the accomplishments of mid-latitude super dual auroral radar network (superdarn) hf radars. *Progress in Earth and Planetary Science*, *6*(1), 27. https://doi.org/10.1186/s40645-019-0270-5

Obayashi, T., & Nishida, A. (1968). Large-scale electric field in the magnetosphere. *Space Science Reviews*, *8*(1), 3–31. https://doi.org/10.1007/BF00362569

Parker, E. N. (1996). The alternative paradigm for magnetospheric physics. *Journal of Geophysical Research*, *101*(A5), 10587–10625. https://doi.org/10.1029/95JA02866

Parker, E. N. (1997). Reply [to "comment on "the alternative paradigm for magnetospheric physics" by e. n. parker"]. *Journal of Geophysical Research*, *102*(A5), 9657–9658. https://doi.org/10.1029/97JA00347

Pierrard, V., Botek, E., Ripoll, J.-F., Thaller, S. A., Moldwin, M. B., Ruohoniemi, M., & Reeves, G. (2021). Links of the plasmapause with other boundary layers of the magnetosphere: Ionospheric convection, radiation belt boundaries, auroral oval. *Frontiers in Astronomy and Space Sciences*, *8*, 728531. https://doi.org/10.3389/fspas.2021.728531

Provan, G., Lester, M., Mende, S., & Milan, S. E. (2004). Statistical study of high-latitude plasma flow during magnetospheric substorms. *Annales Geophysicae*, *22*(10), 3607–3624. https://doi.org/10.5194/angeo-22-3607-2004

Rankin, R., Kabin, K., Lu, J. Y., Mann, I. R., Marchand, R., Rae, I. J., et al. (2005). Magnetospheric field-line resonances: Ground-based observations and modeling. *Journal of Geophysical Research*, *110*(A10), S09. https://doi.org/10.1029/2004JA010919

Ruohoniemi, J. M., & Baker, K. B. (1998). Large-scale imaging of high-latitude convection with super dual auroral radar network HF radar observations. *Journal of Geophysical Research*, *103*(A9), 20797–20811. https://doi.org/10.1029/98JA01288

Sandhu, J. K., Rae, I. J., Staples, F. A., Hartley, D. P., Walach, M.-T., Elsden, T., & Murphy, K. R. (2021a). The roles of the magnetopause and plasmapause in storm-time ulf wave power enhancements. *Journal of Geophysical Research: Space Physics*, *126*(7), e2021JA029337. https://doi.org/10.1029/2021JA029337

Sandhu, J. K., Rae, I. J., & Walach, M.-T. (2021b). Challenging the use of ring current indices during geomagnetic storms. *Journal of Geophysical Research: Space Physics*, *126*(2), e2020JA028423. https://doi.org/10.1029/2020JA028423

Sandhu, J. K., Rae, I. J., Wygant, J. R., Breneman, A. W., Tian, S., Watt, C. E. J., et al. (2021c). Ulf wave driven radial diffusion during geomagnetic storms: A statistical analysis of van allen probes observations. *Journal of Geophysical Research: Space Physics*, *126*(4), e2020JA029024. https://doi.org/10.1029/2020JA029024

Sangha, H., Milan, S. E., Carter, J. A., Fogg, A. R., Anderson, B. J., Korth, H., & Paxton, L. J. (2020). Bifurcated region 2 field-aligned currents associated with substorms. *Journal of Geophysical Research: Space Physics*, *125*(1), e2019JA027041. https://doi.org/10.1029/2019JA027041

Shepherd, S. G. (2014). Altitude-adjusted corrected geomagnetic coordinates: Definition and functional approximations. *Journal of Geophysical Research: Space Physics*, *119*(9), 7501–7521. https://doi.org/10.1002/2014JA020264

Shepherd, S. G., & Ruohoniemi, J. M. (2000). Electrostatic potential patterns in the high-latitude ionosphere constrained by superdarn measurements. *Journal of Geophysical Research*, *105*(A10), 23005–23014. https://doi.org/10.1029/2000JA000171

Sofko, G. J., Greenwald, R., & Bristow, W. (1995). Direct determination of large-scale magnetospheric field-aligned currents with superdarn. *Geophysical Research Letters*, *22*(15), 2041–2044. https://doi.org/10.1029/95GL01317

Stern, D. P. (1977). Large-scale electric fields in the earth's magnetosphere. *Reviews of Geophysics*, *15*(2), 156–194. https://doi.org/10.1029/RG015i002p00156

SuperDARN Data Analysis Working Group, Thomas, E. G., Ponomarenko, P. V., Billett, D. D., Bland, E. C., Burrell, A. G., et al. (2018). Superdarn radar software toolkit (rst) 4.2. https://doi.org/10.5281/zenodo.1403226

SuperDARN Data Analysis Working Group, Thomas, E. G., Ponomarenko, P. V., Bland, E. C., Burrell, A. G., Kotyk, K., et al. (2018). Superdarn radar software toolkit (rst) 4.1. https://doi.org/10.5281/zenodo.1143675

Thomas, E. G., & Shepherd, S. G. (2018). Statistical patterns of ionospheric convection derived from mid-latitude, high-latitude, and polar superdarn hf radar observations. *Journal of Geophysical Research: Space Physics*, *123*(4), 3196–3216. https://doi.org/10.1002/2018JA025280

Vasyliunas, V. M. (2001). Electric field and plasma flow: What drives what? *Geophysical Research Letters*, *28*(11), 2177–2180. https://doi.org/10.1029/2001GL013014

Vasyliunas, V. M. (2005). Relation between magnetic fields and electric currents in plasmas. *Annales Geophysicae*, *23*(7), 2589–2597. https://doi.org/10.5194/angeo-23-2589-2005

Walach, M.-T., & Fogg, A. (2024a). Combined superdarn and ampere plots. *Zenodo*. https://doi.org/10.5281/zenodo.13493214

Walach, M.-T., & Fogg, A. (2024b). Lower latitude boundaries from AMPERE and SuperDARN. *Zenodo*. https://doi.org/10.5281/zenodo.13495838

Walach, M.-T., & Grocott, A. (2019). SuperDARN observations during geomagnetic storms, geomagnetically active times, and enhanced solar wind driving. *Journal of Geophysical Research: Space Physics*, *124*(7), 5828–5847. https://doi.org/10.1029/2019JA026816

Walach, M.-T., Grocott, A., & Milan, S. E. (2021). Average ionospheric electric field morphologies during geomagnetic storm phases. *Journal of Geophysical Research: Space Physics*, *126*(4), e2020JA028512. https://doi.org/10.1029/2020JA028512

Walach, M.-T., Grocott, A., Staples, F., & Thomas, E. G. (2022). Super dual auroral radar network expansion and its influence on the derived ionospheric convection pattern. *Journal of Geophysical Research: Space Physics*, *127*(2), e2021JA029559. https://doi.org/10.1029/2021JA029559

Walach, M.-T., Grocott, A., Thomas, E. G., & Staples, F. (2022). Dusk-dawn asymmetries in superdarn convection maps. *Journal of Geophysical Research: Space Physics*, *127*(12), e2022JA030906. https://doi.org/10.1029/2022JA030906

Walach, M.-T., Milan, S. E., Yeoman, T. K., Hubert, B. A., & Hairston, M. R. (2017). Testing nowcasts of the ionospheric convection from the expanding and contracting polar cap model. *Space Weather*, *15*(4), 623–636. https://doi.org/10.1002/2017SW001615

Waters, C. L., Anderson, B. J., Green, D. L., Korth, H., Barnes, R. J., & Vanhamäki, H. (2020). Science data products for ampere. In M. W. Dunlop & H. Lühr (Eds.), *Ionospheric multi-spacecraft analysis tools: Approaches for deriving ionospheric parameters* (pp. 141–165). Springer International Publishing. https://doi.org/10.1007/978-3-030-26732-2_7

Waters, C. L., Anderson, B. J., & Liou, K. (2001). Estimation of global field aligned currents using the iridium® system magnetometer data. *Geophysical Research Letters*, *28*(11), 2165–2168. https://doi.org/10.1029/2000GL012725

Weygand, J. M., Ngwira, C. M., & Arritt, R. F. (2023). The equatorward boundary of the auroral current system during magnetic storms. *Journal of Geophysical Research: Space Physics*, *128*(6), e2023JA031510. https://doi.org/10.1029/2023JA031510

Wharton, S. J., Rae, I. J., Sandhu, J. K., Walach, M.-T., Wright, D. M., & Yeoman, T. K. (2020). The changing eigenfrequency continuum during geomagnetic storms: Implications for plasma mass dynamics and ulf wave coupling. *Journal of Geophysical Research: Space Physics*, *125*(6), e2019JA027648. https://doi.org/10.1029/2019JA027648

Wright, A. N., & Elsden, T. (2020). Simulations of mhd wave propagation and coupling in a 3-d magnetosphere. *Journal of Geophysical Research: Space Physics*, *125*(2), e2019JA027589. https://doi.org/10.1029/2019JA027589